ADVANCED MULTI-PHASE FLOW CFD MODEL DEVELOPMENT FOR SOLID ROCKET MOTOR FLOWFIELD ANALYSIS

Contract No. NAS8-39398

Final Report

Prepared for

National Aeronautics & Space Administration

George C. Marshall Space Flight Center

Marshall Space Flight Center, AL 35812

By

Paul Liaw

and

Yen-Sen Chen

Engineering Sciences, Inc.

1900 Golf Road, Suite D

Huntsville, AL 35802

March , 1995

ABSTRACT

A Navier-Stokes code, FDNS, is used to analyze the complicated internal flowfield of the SRM (solid rocket motor) to explore the impacts due to the effects of chemical reaction, particle dynamics, and slag accumulation on the solid rocket motor (SRM). The particulate multi-phase flowfield with chemical reaction, particle evaporation, combustion, breakup, and agglomeration models are included in present study to obtain a better understanding of the SRM design.

Finite rate chemistry model is applied to simulate the chemical reaction effects. Hermsen correlation model is used for the combustion simulation. The evaporation model introduced by Spalding is utilized to include the heat transfer from the particulate phase to the gas phase due to the evaporation of the particles. A correlation of the minimum particle size for breakup expressed in terms of the Al/Al_2O_3 surface tension and shear force was employed to simulate the breakup of particles. It is assumed that the breakup occurs when the Weber number exceeds 6. A simple agglomeration model is used to investigate the particle agglomeration. However, due to the large computer memory requirement for the agglomeration model, only 2D cases are tested with the agglomeration model. The VOF (Volume of Fluid) method is employed to simulate the slag buildup in the aft-end cavity of the RSRM. Monte Carlo method is employed to calculate the turbulent dispersion effect of the particles.

The flowfield analysis obtained using the FDNS code in the present research with finite rate chemical reaction, particle evaporation, combustion, breakup, agglomeration, and VOF models will provide a design guide for the potential improvement of the SRM including the use of materials and the shape of nozzle geometry such that a better performance of the SRM can be achieved. The simulation of the slag buildup in the aft-end cavity can assist the designer to improve the design of the RSRM geometry.

TABLE OF CONTENTS

1.0 INTRODUCTION

1.1 THE NATURE OF THE PROBLEM

It is known that the flowfield of the solid rocket motor is very complicated due to the chemical reaction, particle evaporation, combustion, and breakup, and other complex characteristics like agglomeration and coalescence etc. Because the distribution of the particles affects the performance of the motor, the prediction of the particle effects plays an important role for the SRM design.

Traditionally, metal powders are used in solid propellants for the purpose of increasing the motor specific impulse. High density and high heat of reaction are two factors which contribute to high impulse. It is known that the simulations of internal flowfields of SRM's with Al-based propellants require complex multi-phase, turbulent, and chemical reacting flow models. On the other hand, because of relative velocity and temperature differences between particles and the gas flow, inter-phase drag forces and heat transfer exist. Therefore, the effect of particles on the flowfield has a significant impact. The evaporation of the Al and Al_2O_3 transfers the mass from particulate phase to the gas phase. The combustion of aluminum produces aluminum oxide and releases heat and mass. The breakup of the particles affects the flowfield. It is known that a recirculation zone near the entry of the aft-dome cavity disturbs the flowfield and increases the complexity of interaction between the particle phase and the nozzle inlet section. This interaction will determine the slag agglomeration rate which affects the nozzle erosion and motor performance. All these impacts should be investigated so that a better performance of the SRM can be achieved.

To provide design guides for maintaining high performance of the SRM, an accurate simulation of the gas-particle interaction is very important. Because of the complex flowfield inside the SRM, limited experimental data is available for design purpose. The internal flowfield analysis using a CFD (Computational Fluid Dynamics) method can be utilized to obtain a better investigation for SRM's due to the recent progress in computing power. There has been some research conducted in the past for the SRM internal flowfield analysis using the CFD method.

Madabhushi et al. (Ref. 1) calculated the two-phase aft-dome flowfield of the solid rocket motor. The 19-sec burnback configuration was used for the analysis and no particle trajectories in the aft-dome cavity was provided. This may not reveal the realistic particle effects for the first 19 seconds. Since the particles will accumulate on the wall and change the shape of the flow passage. Due to the large impact of turbulent particles, a full configuration should be used to include the effect of upstream particles. Carrier et al (Ref. 2) investigated the aluminum-oxide-particle field within a long-bore SRM with a simple modeling. The Lagrangian particle tracking method was used in Ref. 2. Lupoglazoff and Vuillpt (Ref. 3) simulated the stability of a 2-D SRM numerically by means of the finite volume explicit predictor-corrector McCormack scheme that solves the Euler equation. Sabnis et al (Ref. 4) used an Eulerian-Lagrangian two-phase approach to model the multi-phase reacting internal flow of a SRM with a metalized propellant. Some other studies in the solid propellant rocket motors have been conducted (Refs. 5-8). However, the realistic applications including the multi-phase flow with chemical reactions, evaporation, combustion, breakup, and agglomeration models were not simulated at the same time to investigate the influence of the particles on the SRM. No details about the effects of the recirculation zone on the motor performance have been revealed. Due to the complex flowfield at the entry of the cavity, more investigation for the aft-dome cavity should be conducted using the numerical approach. Since it is very difficult to measure the data for the internal flow of the solid rocket motor. It is found that the slag buildup in the cavity causes the oscillated pressure and may affect the motor performance. Not many studies have been made to investigate the effects of the slag accumulation.

To explore the impacts due to the effects of chemical reaction, recirculation zone, slag buildup, and particle dynamics, a Navier-Stokes code, FDNS (Refs. 9-11), is used to analyze the complicated flowfield for the SRM with chemical reaction, and particle evaporation, combustion, breakup, and agglomeration models.

1.2 OBJECTIVE

The objective of this project is to develop an advanced particulate multi-phase flow model which can simulate the effects of particle dynamics, chemical reaction and hot gas flow turbulence.

The inclusion of particle evaporation, combustion, breakup, and agglomeration, particle/gas reaction and mass transfer, and slag buildup in modeling the particle dynamics will allow the proposed models to realistically simulate the internal flowfield of a solid rocket motor.

2.0 CFD METHODOLOGY

2.1 GOVERNING EQUATIONS

The FDNS flow solver (Refs. 9-11) provides steady-state and unsteady flowfield solutions by solving the following transport equations. The general form of the mass conservation equation, Reynolds-averaged Navier-Stokes equations, energy equation and other scalar transport equations can be written as:

$$\frac{\partial \rho U}{\partial t} + \frac{\partial}{\partial x_i}\left(\rho u_i U + \mu_e \frac{\partial U}{\partial x_i} \right) = S_U \quad (1)$$

where ρ and U = (1, u, v, w, h, k, ε and α_i) stand for the fluid density and the flow primitive variables for the continuity, momentum, energy, turbulence model and species mass-fraction equations respectively. This general form of the transport equation has one exception that fluid temperature instead of enthalpy is used for the diffusion (heat conduction) terms of the energy equation. The source terms SU for the momentum, energy, turbulence model and species mass-fraction equations in 3-dimensional space x_i can be written for fully conservative form as:

$$S_U = \begin{Bmatrix} M_p \\ -\frac{\partial P}{\partial x_j} + \frac{\partial}{\partial x_i}\left(\mu_e \frac{\partial u_i}{\partial x_j} \right) - \frac{2}{3}\frac{\partial}{\partial x_j}\left(\mu_e \frac{\partial u_i}{\partial x_i} \right) + D_i + M_p V_{p_i} \\ \frac{DP}{Dt} + \Phi + Q_t - V_{p_i} D_i + M_p\left(hv + Ur^2/2 \right) \\ \rho(\mathrm{P_r} - \varepsilon) \\ \rho\frac{\varepsilon}{k}\left[\left(C_1 + C_3 \mathrm{P_r}/\varepsilon \right)\mathrm{P_r} - C_2\varepsilon \right] \\ \omega_n, n = 1, \ldots\ldots N \end{Bmatrix}$$

where $\mu_e = (\mu_l + \mu_t)/\sigma$ represents the effective viscosity which is a sum of the laminar viscosity and the turbulence eddy viscosity then divided by the Schmidt or Prandtl number, σ. Φ, Qt and ωn are the energy dissipation function, heat source and the species source term respectively. Di represents the drag forces. Mp denotes the rate of mass addition per unit volume due to inter-phase mass

exchange. Vi are the particle velocity components. hv stands for the particle vapor enthalpy. Ur is the gas velocity relative to the particle velocity. Pr stands for the turbulence kinetic energy production rate which is written as:

$$P_r = \frac{\mu_t}{\rho}\left\{\frac{1}{2}\left(\frac{\partial u_j}{\partial x_i}+\frac{\partial u_i}{\partial x_j}\right)^2 - \frac{2}{3}\left(\frac{\partial u_k}{\partial x_k}\right)^2\right\}$$

The turbulence modeling constants C_1 and C_2 are given as 1.43 and 1.92 respectively in the standard k-ε turbulence model. For the extended model, $C_2 = 1.90$ is a modeling constant and C_1 takes a functional form as:

$$C_1 = 1.15 + 0.25\,\frac{P_r}{\varepsilon}$$

Turbulence Schmidt numbers for the k- and ε-equation are 1.0 and 1.3 respectively for the standard model. For the extended model these two constants are modified to be 0.8927 and 1.15 respectively. Turbulence Schmidt number for the species mass fraction equation is assumed to be 0.9. The same value is assumed for the energy equation turbulence Prandtl number (0.7 is used for laminar flows). To account for compressibility effect on the turbulence models, two methods of model correction are available in the FDNS code. They are: (1) k-equation correction, in which the dissipation term in the k-equation is modified by a turbulence Mach number; and (2) ε-equation correction, in which the C_1 in the ε-equation is modified by the flow Mach number. An equation of state of the following form is used to calculate fluid density and provide closure to the above governing equations.

$$\rho = \frac{P}{RT / M_w}$$

where R, T and Mw stand for the universal gas constant, fluid temperature and the mixture molecular weight. The fluid temperature is calculated based on the solution of the fluid enthalpy and the JANNAF standard thermodynamics data using a Newton's iteration method for finding the roots of the polynomials.

Particulate-Phase Equations

The equations that constitute the particle trajectory and temperature history can be written as:

$$\frac{DV_i}{Dt} = \left(U_i - V_i\right) / t_d$$

$$\frac{Dh_p}{Dt} = Cp_c\left(T_{aw} - T_p\right) / t_H - 6\sigma\varepsilon f T_p^4 / \left(\rho d\right)_p$$

where

Ui = gas velocity

Vi = particle velocity

td = particle dynamic relaxation time
= $4\rho_p d_p / \left(3Cd\,\rho_c \left|U_i - V_i\right|\right)$

hp = particle enthalpy

Tp = particle temperature

Taw = gas recovery temperature

tH = particle thermal-equilibrium time
= $\left(\rho d\right)_p / \left[12 Nu\,\mu / \left(\mathrm{Pr}\, d_p\right)\right]$

σ = Stefan-Boltzmann constant
= 4.76E-13 BTU/FT^2-S-°R

ε = particle emissivity = 0.20 ~ 0.31

f = radiation interchange factor

Cd and Nu stand for drag coefficient and Nusselt number for heat transfer which are functions of Reynolds number and relative Mach number. Typical correlation are described in references 12 and 13.

Turbulent dispersion

To simulate the turbulent dispersion of particles, the Gaussian probability distribution with standard deviation equal to $(2k/3)^{1/2}$ is used for the random turbulent velocity components. The turbulent velocity components are thus computed using

$$u' = (4k/3)^{1/2} erf^{-1}(2x-1)$$

where x is a random variable with uniform probability distribution between 0 and 1. The generated turbulent velocity components are added to the mean velocity field of the continuous phase in evaluating the interphase drag force.

2.2 NUMERICAL ALGORITHM

The FDNS flow solver is a finite difference method for solving non-linear governing equations using non-staggered curvilinear grid system. This code provides multi-zone multi-block options (Ref. 14) for multiple species and finite rate chemistry reacting flow by solving the Navier-Stokes equations for the simulation of complex geometry flow problems. A Lagrangian-Eulerian particle tracking method is employed in the FDNS to provide effects of momentum and energy exchanges between the gas phase and the particle phase. The particle trajectories are calculated using a one-step implicit method for several groups of particle sizes by which the drag forces and heat fluxes are then coupled with the gas phase equations. A second-order upwind scheme is employed to approximate the convection terms. Viscous fluxes and source terms are discritized using second-order central difference approximation. The time domain discritization of the present method allows the finite difference equations to be arranged into delta form for time-marching integration. Time-centered or Euler implicit time-marching schemes are employed for time accurate or steady-state computations respectively. A CFL number conditioned non-uniform time marching option can also be used for efficient steady-state solutions. The final linearized algebraic equations are solved by iterative point relaxation, ADI or L-U matrix solver. The time-marching scheme is described below. For convenience, transformed equations (from Xi to ξi system with J as the Jacobian of coordinate transformation) of Eq. 1 is written as:

$$\frac{1}{J}\frac{\partial \rho U}{\partial t} = -\frac{\partial F_i}{\partial \xi_i} + S_U = R_U \tag{2}$$

where F represents convection and diffusion fluxes. First, Eq. 2 is discretized in time with a second-order time-centered scheme. That is

$$\frac{1}{J\Delta t}\left\{(\rho U)^{n+1} - (\rho U)^n\right\} = \frac{1}{2}\left(R_U{}^{n+1} + R_U{}^n\right)$$

where superscripts n and n+1 represent old and new time levels respectively. If a sub-iteration procedure within a time step is applied, the following linearization can be incorporated.

$$(\rho U)^{k+1} = (\rho U)^k + \rho^k \Delta U^k$$

$$R_U{}^{k+1} = \left(\frac{\partial R_U}{\partial U}\right)^k \Delta U^k + R_U{}^k$$

where the superscript k denotes the k-th sub-iteration. With the above approximations, the final form of the time-marching scheme can be written as:

$$\left\{\frac{\rho^k}{J\Delta t} - \left(\frac{\partial R_U}{\partial U}\right)^k\right\}\Delta U^k = -\frac{(\rho U)^k - (\rho U)^n}{J\Delta t} + \frac{R_U{}^k + R_U{}^n}{2}$$

The solutions at time level n+1 is then updated by:

$$U^{n+1} = U^{k+1} = U^k + \Delta U^k$$

When k = 1 is selected, a non-iterative time-marching scheme with a multi-corrector solution method can provide time accurate solutions for unsteady flow problems. The pressure based multi-corrector solution method is formulated using simplified perturbed momentum and continuity equations. The simplified velocity correction equation can be written as:

$$\frac{\partial \rho u_i}{\partial t} \approx -\nabla P$$

or, in discrete form,

$$u_i{}' \approx -\beta \frac{\Delta t}{\rho}\nabla P' \quad and \quad P^{n+1} = P^n + P' \tag{3}$$

where β represents a pressure relaxation parameter (typically 10). The velocity and density fields in the continuity equation are then perturbed to form a correction equation. Higher order terms are neglected. That is,

$$\frac{\partial \rho'}{\partial t} + \nabla(u_i \rho') + \nabla(\rho u_i') = -\left(\frac{\partial \rho}{\partial t}\right)^n - \nabla(\rho u_i)^n \tag{4}$$

Substituting Eq. 3 into 4 and letting ρ' = P'/RT, the following all speed pressure correction equation is obtained.

$$\frac{1}{RT}\frac{\partial P'}{\partial t} + \nabla\left(\frac{u_i}{RT}P'\right) - \nabla(\beta \Delta t \nabla P') = -\left(\frac{\partial \rho}{\partial t}\right)^n - \nabla(\rho u_i)^n \tag{5}$$

To provide smooth shock solutions the adaptive dissipation terms based on the pressure field is added to the right hand side of Eq. 5. Once solution of Eq. 5 is obtained, the velocity and pressure fields are updated using Eq. 3. The density field is then updated through the equation of state. The temperature field can also be modified by using a perturbed temperature correction equation. The entire corrector step is repeated 3 or 4 times such that the mass conservation condition is enforced before marching to the next time level.

3.0 PROPOSED MODELS

3.1 FINITE RATE CHEMISTRY MODEL

For gas-phase chemical reaction modeling, a general system of chemical reactions can be written in terms of its stoichiometric coefficients (ν_{ij} and ν_{ij}') and the i-th chemical species name (M_i) of the j-th reaction as

$$\sum_i \nu_{ij} M_i = \sum_i \nu_{ij}' M_i'$$

The net rate of change in the molar concentration of species i due to reactions j, X_{ij}, can be written as:

$$X_{ij} = (\nu_{ij}' - \nu_{ij})(K_{fj} \Pi (\rho \alpha_i / M_{Wi})^{\nu_{ij}} - K_{bj} \Pi (\rho \alpha_i / M_{Wi})^{\nu_{ij}'}]$$

and the species production rate, ω_i, (in terms of mass fraction) is calculated by summing over all reactions.

$$\omega_i = M_{Wi} \sum_j X_{ij}$$

where

M_{Wi} = molecular weight of species i

α_i = mass fraction of species i

ρ = fluid density

K_{fj} = forward rate of reaction j

K_{bj} = backward rate of reaction j = K_{fj}/K_{ej}

K_{ei} = equilibrium constant

$$= (1/RT)^{\Sigma(\nu_{ij}' - \nu_{ij})} EXP\left\{\Sigma\left(f_i' \nu_{ij}' - f_i \nu_{ij}\right)\right\}$$

f_i = Gibbs free energy of species i

$K_f = A T^B EXP(-E/RT)$

Finally, the species continuity equations can be written as:

$$\rho D t \alpha_i - \nabla[(\mu_{eff}/\sigma_\alpha)\nabla\alpha_i] = \omega_i$$

where σ_α (assumed to be 0.9) represents the schmidt number for turbulent diffusion. A penalty function is employed to ensure the basic element conservation constraints at the end of every time marching step. This is a crucial requirement for the numerical stability and accuracy of a CFD combustion model. It is accomplished by limiting the allowable changes in species concentrations, which are the solutions of the species continuity equations, for each time step such that the species mass fractions are well bounded within physical limits. The resulting limited changes are adjusted so that they are proportional to the species source terms.

3.2 COMBUSTION MODEL

The combustion model using Hermsen correlation (Ref. 15) is employed. The complete description of this correlation is described in the following:

$$\frac{d(m_{Al})}{dt} = -\frac{\pi}{2}\rho_{Al}\frac{k}{n}D_p^{3-n}$$

where the exponent n is 1.8, Dp is the particle diameter, ρAl is the density of aluminum, and the burning rate constant k ($cm^{1.8}/s$) in the above equation is computed from

$K = 8.3314 \times 10^{-5} Ak^{0.9} Pc^{0.27} Sh/2$

where Pc is the chamber pressure (psia), Sh is the Sherwood number based on particle diameter, and Ak is a measure of the availability of oxidizing species and is computed using

$$A_k = 100\sum_i X_i \quad ; i = CO_2, H_2O, O_2, OH, O$$

The Sherwood number was computed using empirical correlation relating it to the Reynolds number,

$$Sh_p = 2.0 + 0.6\,\mathrm{Re}_p^{0.5}\,\mathrm{Pr}^{0.687} \quad ; \mathrm{Re}_p \le 278.92$$
$$Sh_p = 2.0 + 0.6\,\mathrm{Re}_p^{0.5}\,\mathrm{Pr}^{0.687} \quad ; \mathrm{Re}_p \ge 278.92$$

The calculated mass loss (m_{Al}) of particles due to the combustion at each time step is used to compute the new particle size. The combustion model is used for the Al particles only. Al particle starts to burn when its surface temperature exceeds its melting point. The diameter of Al particle reduces when it burns and the aluminum oxide is formed on the particle surface. It is assumed that the combustion stops when the particle diameter is reduced to 50μm. The aluminum becomes aluminum oxide with diameter of 50μm when the combustion stops.

The calculated mass loss at each time step is used to compute the new particle size. For this study, D_{43}, the mean diameter of particle at the nozzle exit is used to determine when the combustion is completed.

$$D_{43} = 3.6304\, D_t^{0.2932}\,(1 - e^{-0.000816\,\varepsilon\,P\,\tau})$$

where

D_{43} = mass-weighted average diameter, μm.

D_t = nozzle throat diameter, in.

ε = Aluminum concentration in chamber, g-mole/100g.

P = chamber pressure, psia.

τ = average chamber residence time, msec.

3.3 EVAPORATION MODEL

For gas temperature exceeding the metal particle boiling point (e.g. 2750 °K for aluminum oxide particle under 1 atm pressure), inter-phase mass transfer can occur through evaporation or

dissociation processes. A commonly adopted treatment for evaporating particles can be summarized as follows:

The mass transfer rate from the discrete particle to the primary gas phase associated with the evaporation is given by Ref. 16:

$$Mp = (\pi/2)\, \rho_p\, d_p^2\, (Dd_p/Dt) = 2\pi d_p (K/Cp) \ln(1 + B)$$

where

Mp = particle mass transfer rate due to evaporation

K = thermal conductivity of continuous phase

Cp = specific heat of continuous phase

B = mass transfer number, $Cp_{,v}(T_\infty - T_w)/L$

$Cp_{,v}$ = specific heat of vapor

T_∞ = ambient temperature of continuous phase

T_w = particle surface temperature

L = latent heat of vaporization at temperature T_w

The evaporation rate Mp will be reduced when the aluminum oxide shell forms on the particle surface due to the combustion. A correction factor depending on the thickness of the shell is applied to include the effect of the oxide shell on the evaporation. The evaporation model is used for Al_2O_3 particles due to the lack of latent heat of vaporization of Al.

3.4 BREAKUP MODEL

This model uses Weber number to determine if the breakup of the particle occurs. After the particle temperature reaches the melting point of Al_2O_3 and AL, the liquid Al_2O_3 and AL could break up based on the Weber number (Ref. 17):

$$We = Dp\, \rho g\, (Ug - Up)^2 / \sigma$$

where

σ = the surface tension,

We = the critical Weber number for particle breakup.

Dp = diameter of particle/agglomerate

ρg = density of gas phase

Ug = velocity of gas phase

Up = velocity of particle/agglomerate

The surface tension of Al_2O_3 at 2,300°K is 0.69 N/m (summarized in Ref. 18). The surface tension of AL is between 0.85 and 0.90 N/m in the temperature range of 970 to 1,020 °K (tabulated in Ref. 18 and 19). For this study, 0.75N/m for the temperature less than 2,300°K and 0.65 N/m for the temperature less than 2,300°K are assumed to determine the surface tension for Al_2O_3 particles/agglomerates. Linear interpolation/extrapolation is used to compute the surface tension of AL particles based on the known data. It is known that for low Weber numbers, droplets are spherical. They tend to distort when the Weber number exceeds about 4. The distortion increases with increasing Weber number until breakup occurs in the range of We = 20 ~ 30. We = 6 is used for current study.

The breakup time of a droplet suddenly exposed to a gas stream has been approximated as (Ref. 20):

$$t_b \approx \frac{d_{ag}}{2(u_g - u_{ag})}\left(\frac{\rho_{ag}}{\rho_g}\right)^{1/2}$$

t_b is approximately 0.1 ms, which is very consistent with the breakup events observed in the experiments conducted in Ref. 20.

3.5 AGGLOMERATION MODEL

The transient simulation is needed for the particle agglomeration. Due to the large computer memory requirement for using the Lagramgian method to simulate the particle agglomeration, assumptions for the agglomeration model are needed:

(1) Agglomeration model is turned on after the statistic particle trajectories are determined using the combustion, evaporation, and breakup models.

(2) Agglomeration occurs only when Weber number is less than 5 and the distance between two particle centers are shorter than 3 quarters of the sum of their radii.

(3) The particles merged together and the new diameter is computed based on the total mass of the merged particles.

Summary of the models

Figure 1 illustrates the models of combustion, evaporation, breakup, and agglomeration used in present study. The aluminum particles (Al) with 150μm combust and forms the aluminum oxide (Al_2O_3) while the diameter is reduced due to the combustion and evaporation. The combustion model is turned off when the diameter of the particle is less than 50μm. The particle is considered as aluminum oxide when its diameter is less than 50μm. The size of the aluminum oxide keeps shrinking because of evaporation and breakup. When the diameter of the particle reduces to 5μm, which is assumed as the maximum diameter of the smoke, the size will not change any more. The particle agglomeration occurs when the conditions described in 3.5 are satisfied.

3.6 VOF MODEL

The VOF (Volume Of Fluid, Refs. 21 and 22) method is used to account for the effect of slag buildup in the aft end region. VOF method can be used to predict the sloshing dynamics, in response to the flight dynamics and local acceleration of the slag in the aft end region.

Traditionally, VOF methods are mainly developed and used for low-speed flows such that incompressibility can be assumed. The incompressible flow assumption has limited their capability. To generalize, the present formulation is based on compressible flow governing equations. The forms of the equations are then continuously reduced to their incompressible forms according to the local flow conditions and the VOF solutions. To illustrate this, a general transport equation can be written as:

$$\frac{\partial \rho \phi}{\partial t} + \frac{\partial \rho \left(u - u_g\right)_i \phi}{\partial x_i} = S_\phi \qquad (6)$$

And, the VOF transport equation is given below:

$$\frac{\partial \alpha}{\partial t} + \left(u - u_g\right)_i \frac{\partial \alpha}{\partial x_i} = S_\alpha$$

where $\alpha = 1$ stands for liquid and $\alpha = 0$ is for gas. The interface is located at $1 > \alpha > 0$. For a given solution of α field, equation (6) can be recast as:

$$\frac{\partial \rho_m \phi}{\partial t} + \frac{\partial \rho_m \left(u - u_g\right)_i \phi}{\partial x_i} = S_\phi, \quad \alpha > 0.01 \quad \text{-------} \textit{for compressible gas}$$

$$\rho_m \frac{\partial \phi}{\partial t} + \rho_m \left(u - u_g\right)_i \frac{\partial \phi}{\partial x_i} = S_\phi, \quad \alpha \le 0.01 \quad \text{-------} \textit{for incompressible gas}$$

and

$$\rho_m = Max\left\{\rho_g, \alpha \rho_\ell\right\}$$

where ρ_g and ρ_l denote gas and liquid density respectively. u_g represents the grid speed components used to simulate moving domain effects. The numerical accuracy of the VOF method depends highly on the interface resolution. To prevent the solution from becoming too smearing due to numerical diffusion, a compression procedure is developed to perform VOF interface

rescaling such that the total volume within the interface ($0.1 < \alpha < 0.9$) is kept constant through out the computation. The interface α solution compression procedure is expressed as:

$$\alpha_{new} = Max\left\{0, Min\left[1, 0.5 + f\left(\alpha_{old} - 0.5\right)\right]\right\}$$

and

$$f = \frac{\left(Interface\ volume\right)_{new}}{\left(Interface\ volume\right)_{initial}}$$

The surface tension forces in the continuum surface force model is formulated as continuous body forces across the interface. These forces can be written as:

$$F_x = -\sigma\left(\nabla \hat{n}\right)\alpha_x$$

$$F_y = -\sigma\left(\nabla \hat{n}\right)\alpha_y + \left(\frac{|\alpha_y|}{y}\right)_{for\ 2D\ axisymmetric\ only}$$

$$F_z = -\sigma\left(\nabla \hat{n}\right)\alpha_z, \text{----} for\ 3D\ case\ only$$

where

σ = surface tension constant

$$\nabla \hat{n} = \hat{\alpha}_{xx} + \hat{\alpha}_{yy} + \hat{\alpha}_{zz}$$

α is 0.5 for the free surface. The VOF method is used to represent the tracking of the free surface between the liquid and gas phase.

4.0 NUMERICAL RESULTS

To test the proposed models, a simple 2-D motor, the 2D ASRM, the 3D ASRM, and a 2D RSRM are used for present study. The computational results show that a recirculation zone exists at the entry of the aft-dome cavity. The particle impingement could cause erosion and damage the nozzle wall. The particles may accumulate in the impingement area and change the wall shape and affect the performance of the motor. The accumulation of the slag in the aft-end cavity may affect the performance of the solid rocket motor. The flowfield is disturbed by the particles and the slag. The pressure jump due to the slag accumulation is captured in the present study. The obtained results are comparable to the known data. The phenomenon is reasonable based on the physical point of view and available experimental data.

4.1 2-D NOZZLE

A simple 2-D axisymmetric solid rocket motor configuration (Fig. 2) of 81x 31 grid points generated with algebraic method is used for present study. Launch conditions with 1g gravity force at 1 atm are considered. The gas phase flow with chemical reaction using 7 species (H2O, O2, H2, O, H, OH, and N2) with 9-step chemical reaction is simulated for the 2-D SRM geometry with and without three groups of particles respectively.

(1) Without particles

The Mach number distributions without chemical reaction and particle effects are shown in Fig. 3. The flow accelerates because of the mass flow issuing from the propellant surface. It is seen that Mach number reaches 1.0 at the nozzle throat. The maximum Mach number of 3.91 at the nozzle exit is reached. Figure 4 shows the Mach number contributions with the simulation of chemical reaction. The maximum Mach number is reduced to 3.642 due to the effect of the heat.

The flowfield is smooth without the effects of particles. Figure 5 illustrates the pressure contours without the effects of chemical reaction and particles. The constant pressure contours in the chamber at each cross station is obtained. The maximum chamber pressure is 929.6psi. The pressure contours with the effect of chemical reaction are shown in Fig. 6. The maximum chamber pressure is increased to 943.3psi due to the effect of chemical reaction. The obtained pressure distributions are also comparable to that of the regular SRM. Lower temperature is obtained (shown in Fig. 7) for the case without chemical reaction. While higher temperature due to the effect of the chemical reaction is shown in Fig. 8. This phenomenon is reasonable.

(2) With particles

Based on the observation by Price (Ref. 23), three major particle groups injecting from the grain surface are assumed to simulate the particulate phase. Particles with diameter of 150 or 175μm represent the Al particles which burns on the grain surface. The second group of particles with diameter of 50μm is assumed to represent the aluminum oxide (Al_2O_3) which is the product due to the combustion of Al on the propellant surface. The third group of particles is the "smoke" which has maximum diameter of 5μm. It is assumed that the "smoke" does not evaporate, combust, break up, and agglomerate. All three groups are injected from the propellant grain surface vertically into the chamber. In order to make comparison, a test case without combustion/evaporation/breakup/agglomeration models is also conducted.

Figure 9 illustrates the trajectories of three groups of particles. It is seen that the size of each particle group is constant. The models of combustion/evaporation/breakup are then used for the test. Figure 10 illustrates the particle trajectories due to the effects of combustion, evaporation, and breakup models. The aluminum particles (Al) with diameter of 150μm combust and form the

aluminum oxide (Al_2O_3) while the diameter is reduced due to the combustion and evaporation. Because of the high temperature in the chamber, Al particle becomes Al_2O_3 within a short period of time after leaving the propellant surface. The Al_2O_3 oxide with diameter larger than 5μm does not burn but will evaporate and may break up. The burning time of the Al particle is longer for those particles coming out of the propellant surface in lower-temperature areas near the nozzle. It is noted that the particle trajectories are not plotted at each time step. The Al_2O_3 particle is accelerated when it approaches the nozzle. The relative speed of the particle and the flow and the change of particle surface tension due to the temperature difference allow particles to break. It is seen that most of the Al_2O_3 particles break up at the nozzle throat. This phenomenon is identical to the experimental data shown in Ref. 17. The breakup model requires large agglomerates formed before the agglomerates enter the nozzle. Experimental data of Ref. 17 demonstrates that the breakup occurs mostly near the throat. The computed results shown in Fig. 11 using current models match the experimental conclusion in Ref. 17. The average of the particle diameter reduced to less than 10μm after the nozzle throat. The agglomeration model is tested and shown in Fig, 12. The Al_2O_3 particle agglomerates are based on the Weber number and the distance between the particles. The particles merge together and become larger when they agglomerate. Figure 12 demonstrates the computational results. It is noted that only few groups are shown in Fig. 12, because it is very difficult to show the particle trajectories for particle agglomeration. The mean particle size distributions shown in Fig. 13 are used to estimate the averaged particle size. It is seen that the size of the particles becomes less than 10μm after they pass the nozzle throat. Figure 14 shows the Mach number contours due to the effects of chemical reaction and particles. The effects of particles on the flow field is clearly seen by comparing Fig. 14 and Fig. 3. Mach number is reduced due to the drag of particles. Apparently, the flowfield is disturbed by the particles, i.e., the

flow speed is reduced due to the effect of particle concentrations away from the center line. The maximum Mach number at the nozzle exit reduced to 3.38 from 3.91. Pressure contours are shown in Fig. 15. Higher pressure (99.6atm) is obtained with the particle effects. This is one of the reasons why Al is used for one of the propellant ingredients. Higher pressure in the chamber can provide more power for the SRM. Figure 16 shows the temperature contours. The temperature is higher due to the heat release from the particles. The increase of the temperature due to the effects of particles is about 163°R. The temperature contours also depend on the particle concentrations. A constant temperature contour in the chamber exists due to the effects of particles. This constant temperature contour line across the chamber should not exist if a more accurate analysis using various initial particle size distributions on the propellant surface is performed.

4.2 2-D ASRM

A simplified 2-D ASRM geometry with axisymmetric flow assumption at launch condition (1-g gravity is assumed) is used for the present study. Figure 17 shows the ASRM configuration. Figure 18 shows the grid system of the 2-D ASRM geometry including the front grain port, the inhibitors, and the aft-end cavity. Algebraic method was used to generate the grids. The geometry and mass flow rate information are provided by the NASA Marshal Space Flight Center. The gas phase flow with chemical reaction using 12 species (H2O, O2, H2, O, H, OH, CO, CO2, CL, CL2, HCL, and N2) and 18-step chemical reactions is simulated for the 2D ASRM geometry.

(1) Without particles

The Mach number distributions without chemical reaction and particles are shown in Fig. 19. The maximum Mach number is about 3.406 at the nozzle exit. The effect of chemical reaction on the Mach number is shown in fig. 20. The Mach number is reduced to 3.15. The pressure contours are shown in Fig. 21. The maximum pressure is 924psi in the combustion chamber. The

temperature is about 6,314°K in the combustion chamber. The velocity vectors near the aft-end cavity are shown in Fig. 23. The recirculation zone near the entry of the cavity is captured. It is believed that the impingement of the particles in this area may cause the erosion, damage the nozzle surface, and affect the performance of the motor.

(2) With particles

The particle trajectories without combustion/evaporation/breakup/agglomeration models near the front grain port, the first inhibitor, and the nozzle are shown in figures 24, 25, and 26 respectively. It is noted that the particles numbers are less and the particle sizes are smaller in fig. 26 in order to have a clear picture. It shows that the upstream particles affect the downstream flowfield. The flow speed in the cavity is very low. Due to the pressure gradient, a recirculation zone is formed near the entry of the cavity. The flow recirculation is the mechanism to change the particle trajectories. The particles are turned due to the recirculation and travel along the grain surface through the cavity and into the nozzle. Because of the unstable nature of the flow in the cavity, the steady solution can not be obtained for the flowfield inside the cavity. These show the complicated flow phenomena in the area near the cavity and the nozzle.

Figure 27 illustrates the mean particle size distributions near the nozzle using combustion, evaporation, breakup, and agglomeration models. It is seen that the maximum particle size is about 48μm. The particles size become smaller due to the breakup at the nozzle throat. The maximum particle size at the nozzle is about 20μm. The larger particles come from the grain surface near the entry of the nozzle. A more accurate set of initial conditions of the grain surface is required to obtain a better simulation. Figure 28 shows the Mach number distributions near the nozzle. Apparently, the flowfield is disturbed by the particles, i.e., Mach number distributions in the nozzle are deformed and the flow speed is reduced due to the effect of particle concentrations away from

the center line. The Mach number is less than 0.35 in the chamber and ranges from 2.65 to 3.01 at the nozzle exit

4.3 3D ASRM

The 3D ASRM geometry with axisymmetric flow assumption at launch condition (with 1-g gravity) is used for the present study. Figure 29(a) shows the grid system of the 3D ASRM geometry including the front grain port, the inhibitors, and the aft-end cavity. Only one eleventh of the whole geometry is simulated due to the symmetric geometry. Figure 29(b) illustrates the domain near the front grain port and the first inhibitor. Figure 29(c) illustrates the domain near the aft-dome cavity and the submerged nozzle. It notes that Figure 29 is a rough schematic illustration showing how the grids are distributed. An algebraic method was used to generate the grids. 64,152 grid points are used for the whole grid system. The gas phase flow with chemical reaction using 12 species (H2O, O2, H2, O, H, OH, CO, CO2, CL, CL2, HCL, and N2) and 18-step chemical reactions is simulated for the 3D ASRM geometry with and without particles respectively.

(1) Without particles

The test is first conducted for the case with chemical reaction and without particles. The Mach number distributions are shown in Figure 30. It is seen that Mach number reaches 1.0 at the nozzle throat. Very low Mach number is obtained near the front grain port. The flowfield near the end of the front grain port is disturbed due to the flow coming out of the grain slots. The Mach number is less than 5.6 in the combustion chamber. The flow accelerates and reaches the maximum Mach number of 3.508 at the nozzle exit. The pressure contours are shown in Fig. 31. More complicated pressure distributions near the end of the front grain port and the entry of the aft-end cavity are captured. The geometry change in these areas causes the flow disturbance. The simulated chamber pressure is about 1,200psi. Figure 32 shows the temperature distributions. The maximum

temperature is about 6,314°R in the combustion chamber and reduced to about 2,700°R at the nozzle exit. Figure 33 demonstrates the flowfield near the aft-end cavity. A strong recirculation zone is captured. The strong impingement will cause the damage to this area and affect the motor performance.

(2) With particles

The particle trajectories are shown in fig. 34 for the whole domain. Figure 35 illustrates the particle trajectories and velocity vectors near the front grain port. The particles are driven by the flow field. It is seen that the particles do not accelerate in the low speed zone near the front of the grain port. The particles accelerate and come out of the grain port slot as shown in Fig. 35(a). This is demonstrated by the velocity vectors shown in Fig. 35(b) and (c). Figure 36(a) illustrates the particle trajectories near the first inhibitor. The particles coming out of the inhibitor are affected by the flow field in the chamber as shown. Figure 36(b) shows the velocity vectors near the first inhibitor. It is seen that the flowfield of the combustion chamber is affected by the flow coming out of the inhibitor.

Figure 37 shows the complicated unsteady flow characteristics in the aft-end cavity. The particles may become slag and accumulate in the cavity. This will affect the motor performance. The flow speed in the aft-end cavity is very low. Due to the pressure gradient, a recirculation zone is formed at the entry of the cavity. The flow recirculation is the mechanism to change the particle trajectories. The particles are turned due to the recirculation and travel along the grain surface through the cavity and into the nozzle. Some particles go into the cavity after impinging to the nozzle wall. This impingement could damage the nozzle wall. Also, an agglomerate could occur on the wall and affect the motor performance. Because of the unstable nature of the flow in the cavity,

study. No evaporation/combustion/breakup/agglomeration models are applied. Only the qualitative analysis is attempted.

(1) Without particles

Figures 42, 43, and 44 show the contours of Mach number, pressure, and temperature, respectively. Smooth distributions are obtained without the effects of particles. Maximum pressure is 42.15atm (619.6psi). Maximum temperature is 6,137°R. These are based on the data provided by NASA Marshall Space Flight Center. Figure 45 illustrates the velocity vectors in the aft-end cavity without particles. The vortex and an impinging stagnation point on the wall are predicted. Due to the large flow velocity difference between the chamber and the cavity, a vortex should exist. The predictions of the flowfield near the cavity are reasonable based on the physical phenomena. The impingement may damage the material of the wall and affect the performance of the motor.

(2) With particles

Figure 46 shows that the molten particles may enter the cavity and accumulate on the wall. The slag accumulation depends on the temperature, the vortex strength, and the flight angle. The shape of the aft-end cavity dominates the shape and strength of the vortex. Apparently, the slag accumulation exist in the aft-end cavity as soon as the propellant starts to burn in the aft-end cavity. In order to investigate the effects of the particle size on the slag accumulation, different particle diameters are used for this purpose. Figure 47 demonstrates that the slag flow rate entering the cavity depends on the particle size. It shows that an efficient particle combustion results in less slag accumulation in the aft-end cavity. Also, Fig. 47 shows that a two-way coupling to include the interaction of gas and particles is needed for a better analysis. The effects of the particles on the Mach number and temperature contours are shown in figures 48 and 49, respectively. The contours are affected strongly by the particle concentration. The slag accumulation in the aft-end

cavity will change the particle concentration and affects the flowfield. Figure 50 illustrates this phenomenon. The slag accumulation in the aft-end cavity at different times shown in Fig. 50 clearly demonstrates the effects of the slag on the flowfield. Figure 50(1) shows the initial conditions of the assumed slag accumulation and the particle trajectories near the cavity at t = 0 second. It shows that the particles impinge on the wall near the entry of the lower surface of the cavity. The slag should accumulate in this area. Figure 50(2) (at t = 0.000444 sec) demonstrates this predicted phenomenon. It is seen that particles stick on the wall and form the slag layer. The flowfield will then be disturbed due to this slag accumulation. Figure 50(3) illustrates that more slag accumulated in the cavity at t = 0.0598 sec. The slag accumulated on the upper surface of the cavity. It also shows that the slag buildup in the cavity apparently changes the flowfield of the aft-end cavity. Figure 50(4) shows that the slag starts to flow out of the cavity along the wall at t = 0.3482 sec. The particle concentration near the entry of the nozzle is changed by the slag. The slag in the cavity moves due to the oscillated acceleration. More slag comes out of the cavity as shown in figures 50(5)-(8). The slag grows by the merge of the particles coming from the chamber. It is shown that the particle trajectories differ due to the effects of the slag accumulation. The slag on the upper surface of the cavity moves due to the effects of the flowfield and the acceleration of the flight (also see figures 50(5)-(8)). The slag will finally enter the nozzle and affect the performance of the solid rocket motor. Figure 51 shows the pressure history. The slag accumulation increases the pressure in the cavity . The flight test shows the same trend. It is noted that the predicted results are based on a fixed 2D geometry with particles of 100μm. A better comparison can be made if more information from the test flight can be employed for a 3D test.

5.0 CONCLUSIONS AND DISCUSSION

The obtained computational results using FDNS with the proposed models demonstrate the complex internal flowfield of the solid rocket motor. The prediction of the recirculation zone in the aft-dome cavity, the particle impingement on the wall, the effects of the particles on the flowfield and the slag buildup in the aft-end cavity are very crucial for the improvement of the solid rocket motor performance. The predicted results are comparable to the known design values and the flowfield is reasonable based on the physical point of view. The flowfield analysis using the FDNS code in the present study can provide a design guidance for the solid rocket motor. The obtained results can provide the designers a basic guide line for the use of materials and the design of the geometry. The slag accumulation analysis plays an important role for the SRM design, since the distribution of the slag changes the flowfield at the entry of the nozzle and affects performance of the motor. A better performance of the solid rocket motor can be achieved by modifying the geometry of the aft-end cavity using the CFD method to prevent the formation of vortex and slag accumulation in the aft-end cavity. The geometry of the propellant grain can also be improved using CFD method to increase the combustion efficiency.

6.0 REFERENCES

1. Madabhushi, R, Sabnis, J., Jong, F., and Gibeling, H., "Calculation of the Two-Phase Aft-Dome Flowfield in Solid Rocket Motors," Journal of Propulsion, Vol. 7, NO. 2, March-April 1991, pp. 178-184.
2. Carrier, G., Fendell, F., Brent, D., Kimbrough, C., Loucks, S., Hess, E., and Acotsa, P., "Simple Modeling of Particle Trajectories in Solid Rocket Motors," J. of Propulsion, Vol. 7, NO. 2, March-April, 1991, pp. 185-195.
3. Lupoglazoff, N., and Vuillot, F., "Two-Dimensional Numerical Simulation of the Stability of A Solid Propellant Rocket Motor," AIAA-91-0205, AIAA 29th Aerospace Science Meeting, Reno, Nevada, Jan. 1991.
4. Sabnis, J., Jong, F. de, and Gibeling, H., "A Two-Phase Restricted Equilibrium Model for Combustion of Metalized solid Propellants," AIAA-92-3509, AIAA/SAE/ASME/ASEE 28th Joint Propulsion Conference and Exhibit, Nashiville, TN, July 6-8, 1992.
5. Hsieh K., Yang, V., and Tseng, I., "Navier-Stokes Calculation of Solid Propellant Rocket Motor Internal Flow Fields," AIAA-88-3182, AIAA 24th Joint Propulsion Conference, Boston, July 1988.
6. Culick, F. E. C., "Rotational Axisymmetric Mean Flow and Damping of Acoustic Waves in a Solid Propellant Rocket," AIAA Journal, Vol. 4, No. 8, 1966, pp. 1462-1469.
7. Chang, I., "An efficient Solution for Viscous Flow Inside SRM," AIAA Paper 91-2429, June 1991.
8. Golafshani, M. and Loh, H. T., "Computation of Two-Phase Viscous Flow in Solid Rocket Motors Using a Flux-Split Eulerian-Lagrangian Technique," AIAA Paper 89-2785, July 1989.

9. Chen Y.-S., "Compressible and Incompressible Flow Computations with a Pressure Based Method," AIAA Paper 89-0286, AIAA 27th Aerospace Sciences Meeting, Reno, Nevada, Jan. 1989.

10. Chen Y.-S., "Viscous Flow Computations Using A Second-Order Upwind Differencing Scheme," AIAA Paper 88-0417, AIAA 26th Aerospace Sciences Meeting, Reno, Nevada, Jan. 11-14, 1988.

11. Wang T.-S. and Chen, Y.-S., "A Unified Navier-Stokes Flowfield and Performance Analysis of Liquid Rocket Engines," AIAA Paper 90-2494, AIAA/SAE/ASME/ASEE 26th Joint Propulsion Conference, Orlando, FL, July 16-18, 1990.

12. Carlson, D., and Hoglund, R., AIAA Journal, Vol. 2, NO. 11, Nov. 1964.

13. Henderson, C., AIAA Journal, Vol. 14, NO. 6, June 1976, p. 707.

14. Rhie, C. M., "A Pressure Based Navier-Stokes Solvers Using the Multigrid Method," AIAA Paper 86-0207, AIAA 24th Aerospace Sciences Meeting, Jan. 1986.

15. Hermsen, R. W., "Aluminum Combustion Efficiency in Solid Rocket Motors," AIAA paper 81-0038, January 1981.

16. Spalding, D. B., Proc. 4th Symposium (International) on Combustion, William and Wilkins, Baltimore, MD (1953) 847-864.

17. Caveny, L. H. and Gany, A., "Breakup of Al/Al_2O_3 Agglomerates in Accelerating Flowfields," AIAA Journal, Vol. 17, No. 12, Dec. 1979.

18. Smithells, C. J., "*Metal Reference Book*," Vol. II, 3rd ed., Butterworth & Co., Ltd., London, 1962, p. 685.

19. Brandt, J. L., "Properties of Pure Aluminum," *Aluminum, Vol. 1 Properties, Physical Metallurgy and Phase Diagrams*, edited by K. R. Van Horn, American Society for Metals, Metals Park, Ohio, 1967, pp. 18-19.

20. Harrje, D. T. and Reardon, F. H., Eds., "*Liquid Propellant Rocket Combustion Instability*," NASA SP-194, 1972.

21. Hirt, C. W., and Nichols, B. D., "Volume of Fluid (VOF) Method for the Dynamics of Free Boundaries," Journal of Computational Physics, Vol. 100, pp. 335 - 354, 1992.

22. Nichols, B. D., Hirt, C. W., and Hotchkiss, R. S., "SOLA-VOF: A Solution Algorithm for transient Fluid Flow with Incompressible Flows with Free Surfaces," Los Alamos Lab., LA-8355, Aug., 1980.

23. Price, E. W., "Combustion of Metallized Propellants," Progress in Astronautics and Aeronautics; Fundamentals of Solid Propellant Combustion, Vol. 90, AIAA, New York 1984, PP. 479-513

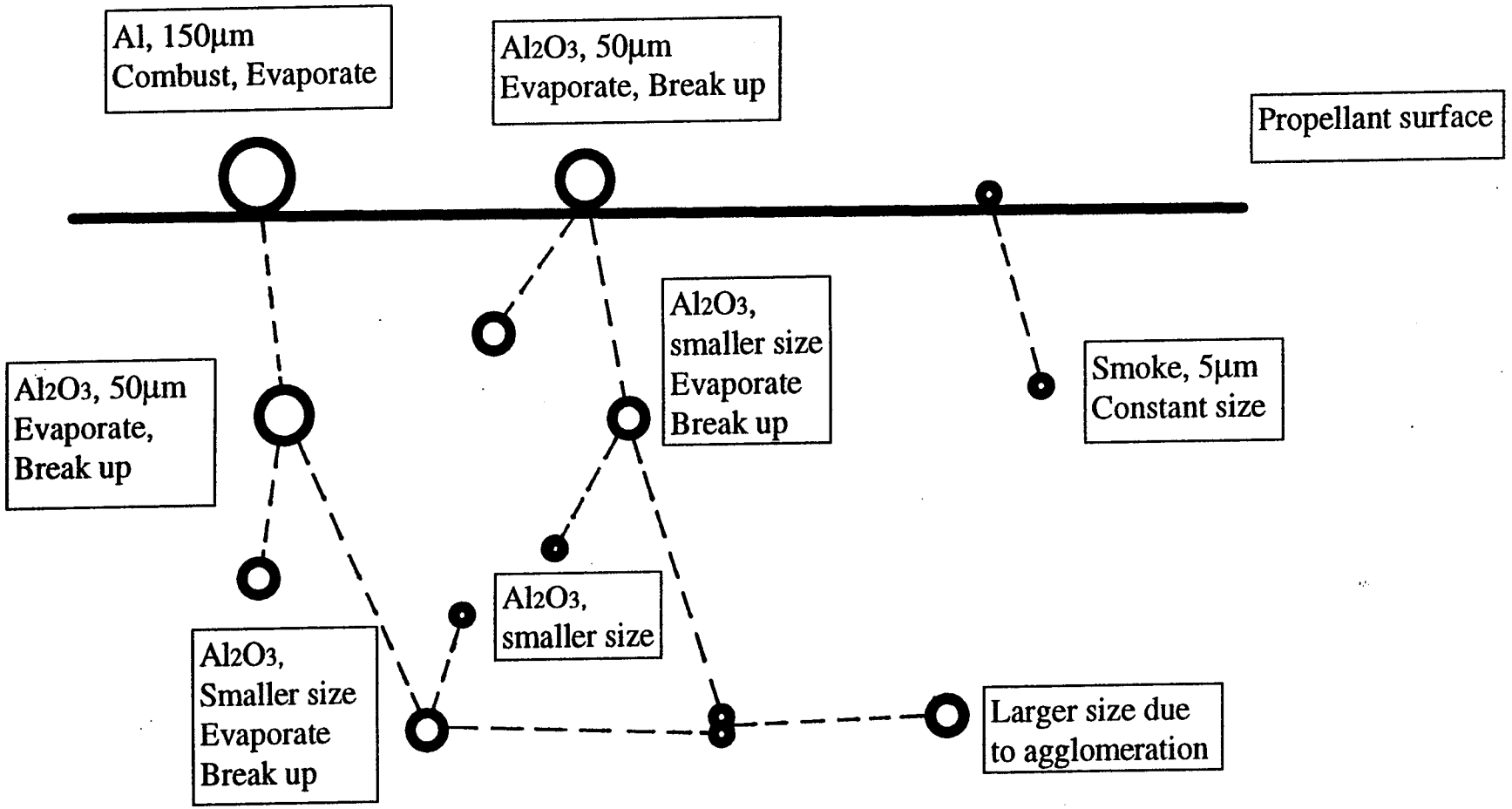

Figure 1 Illustration of combustion, evaporation, breakup, and agglomeration models.

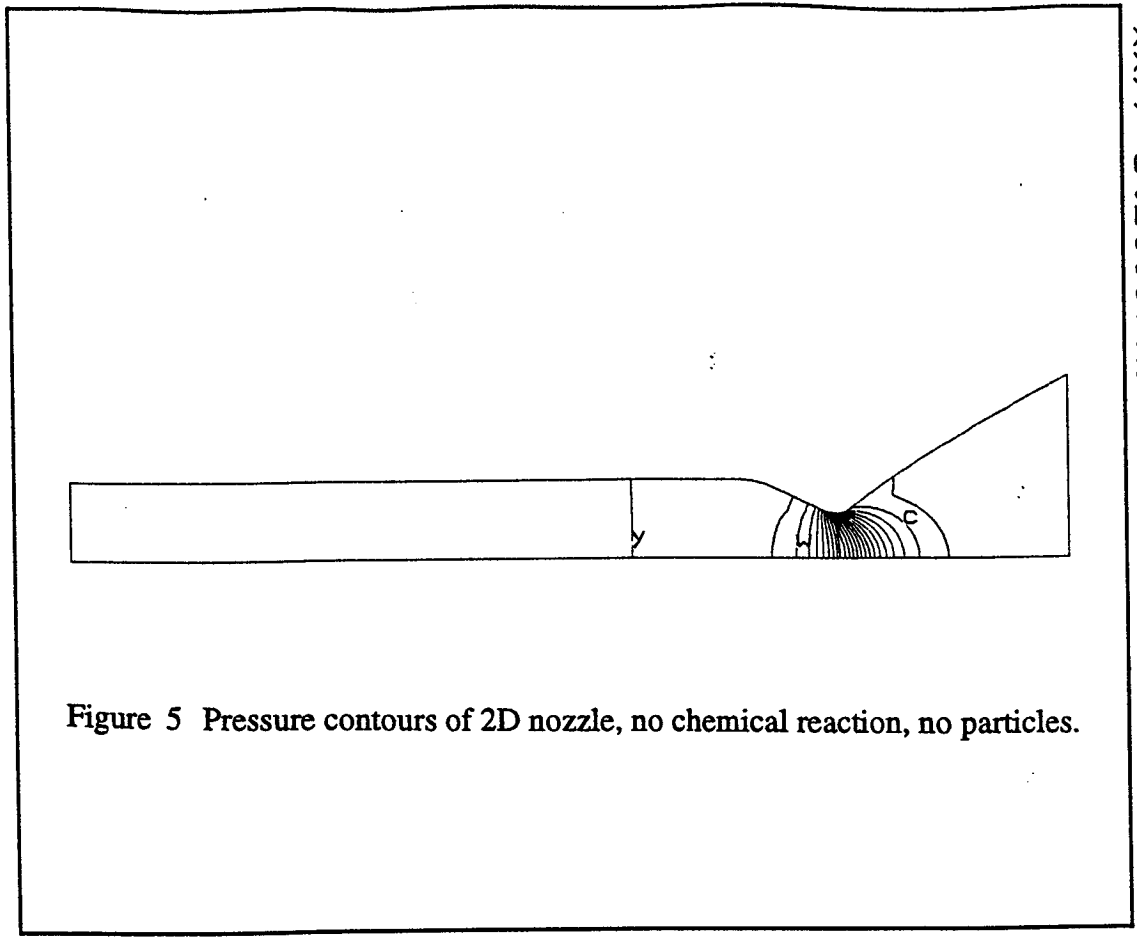

Figure 5 Pressure contours of 2D nozzle, no chemical reaction, no particles.

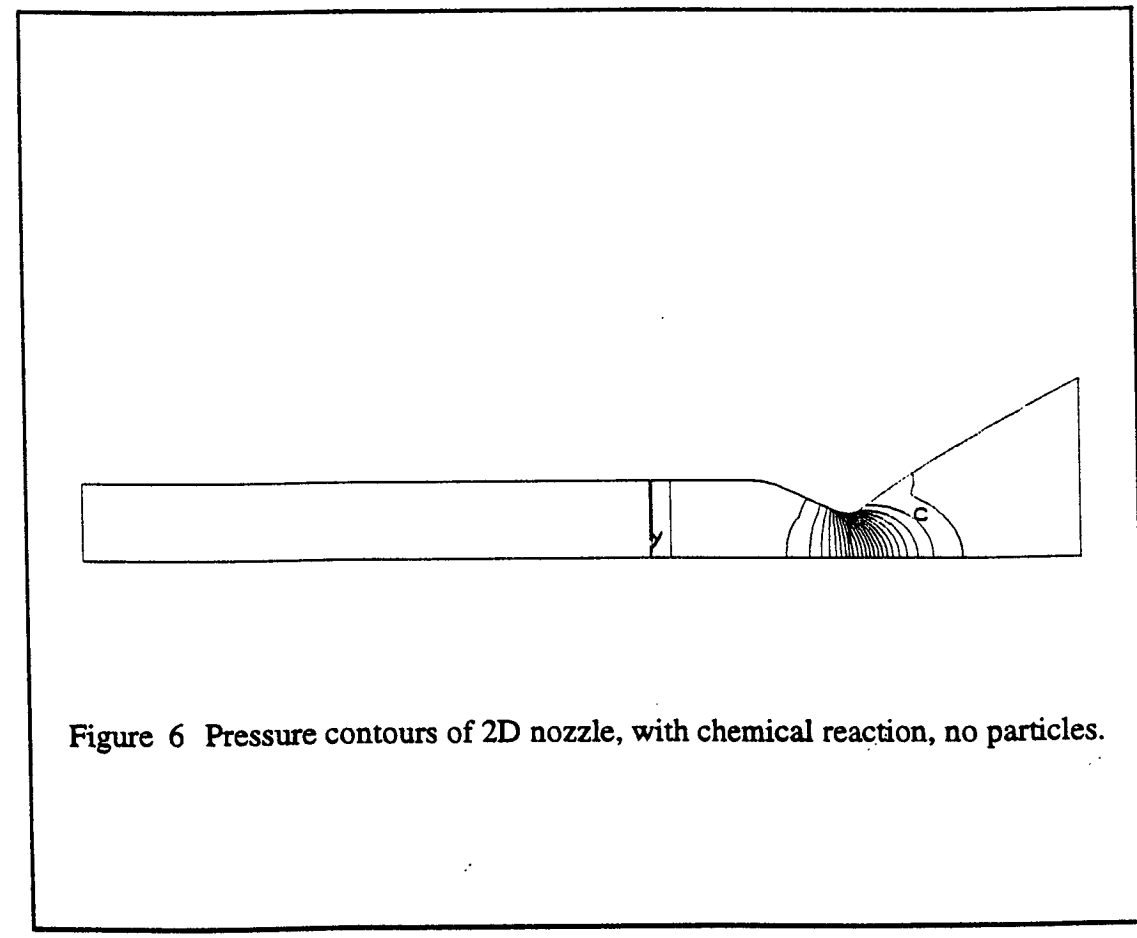

Figure 6 Pressure contours of 2D nozzle, with chemical reaction, no particles.

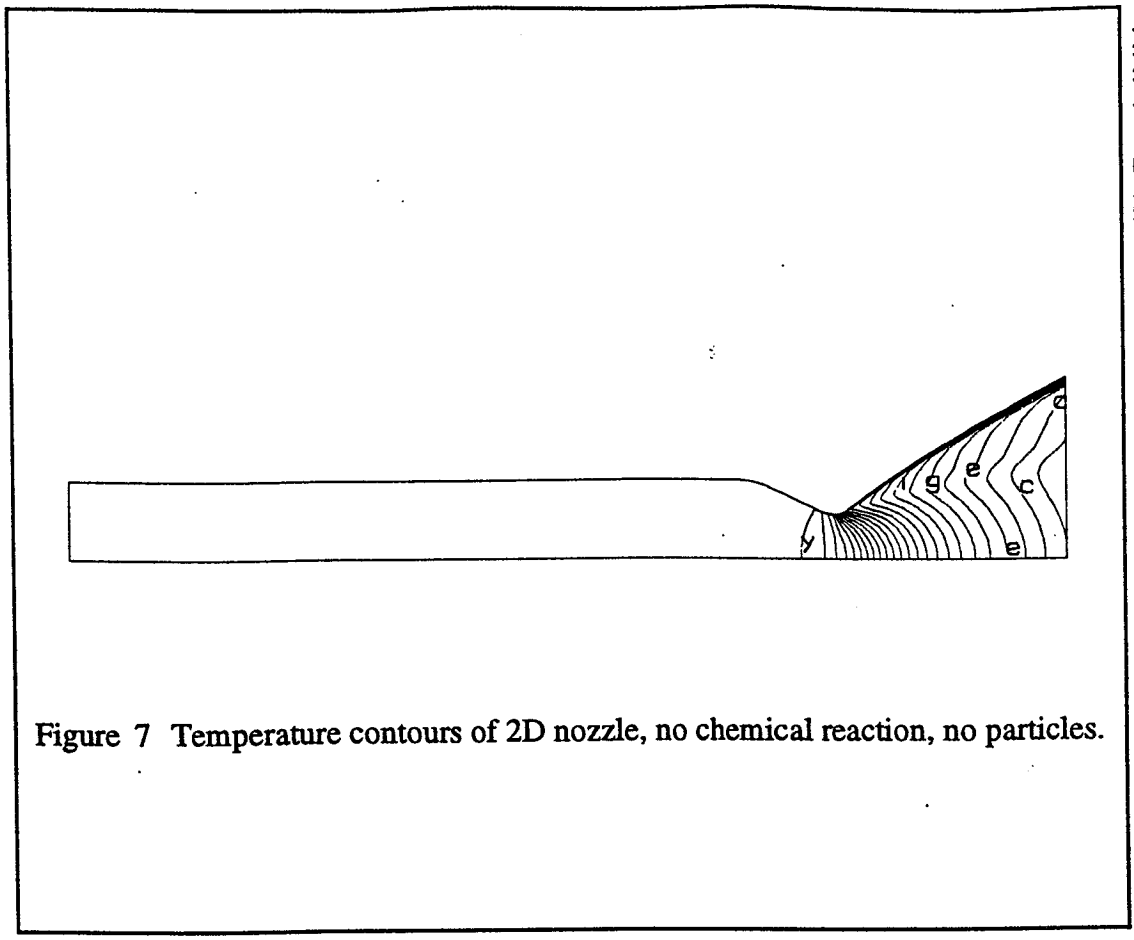

Figure 7 Temperature contours of 2D nozzle, no chemical reaction, no particles.

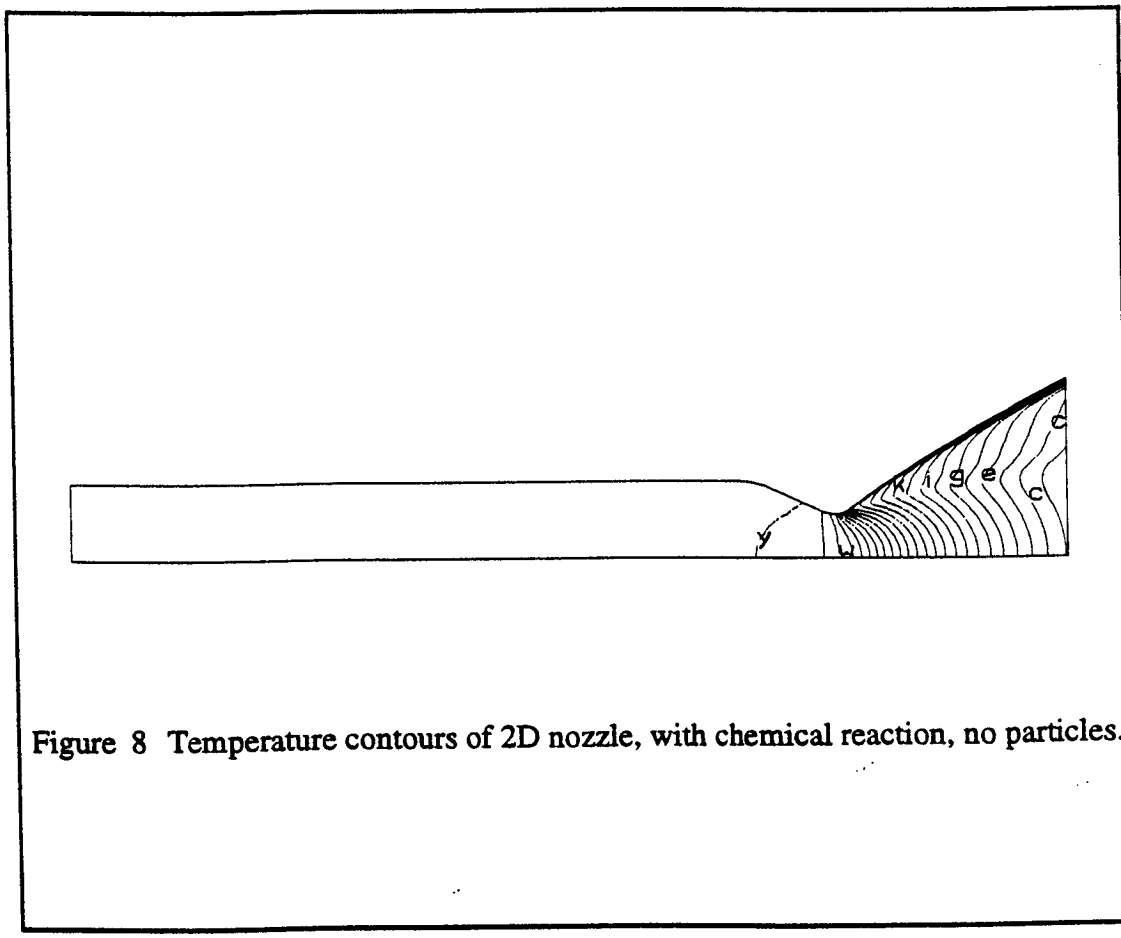

Figure 8 Temperature contours of 2D nozzle, with chemical reaction, no particles.

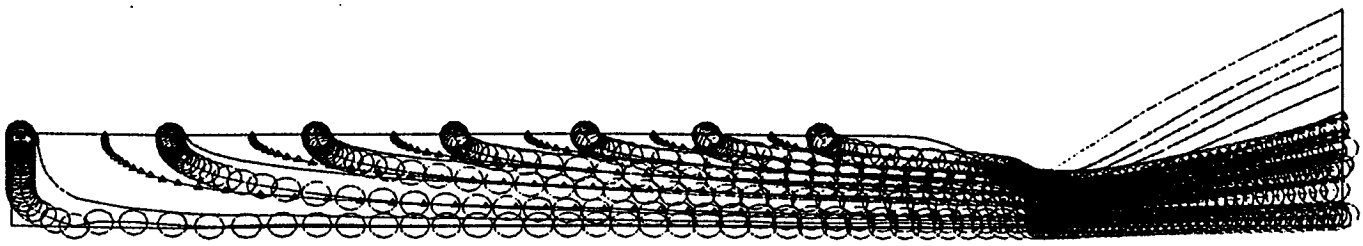

Figure 9 Particle trajectories without combustion/evaporation/breakup models.
Al particle (175μm)
Al_2O_3 particle (50μm)
Smoke (Al_2O_3 particle, 5μm)

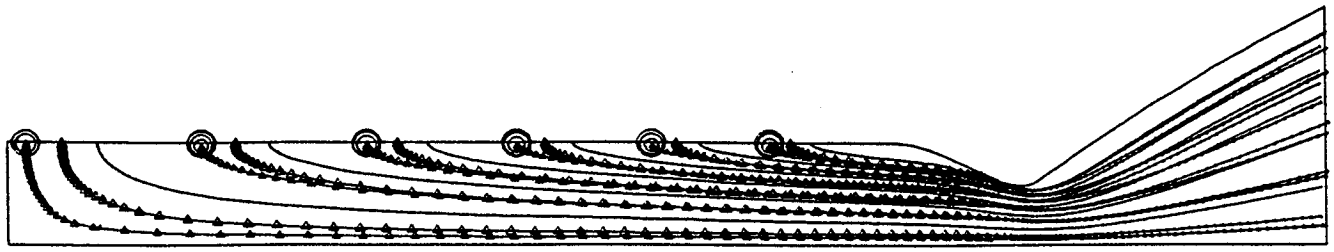

Figure 10 Particle trajectories with combustion/evaporation/breakup models.
Al particle (150μm)
Al_2O_3 particle (50μm)
Smoke (Al_2O_3 particle, 5μm)

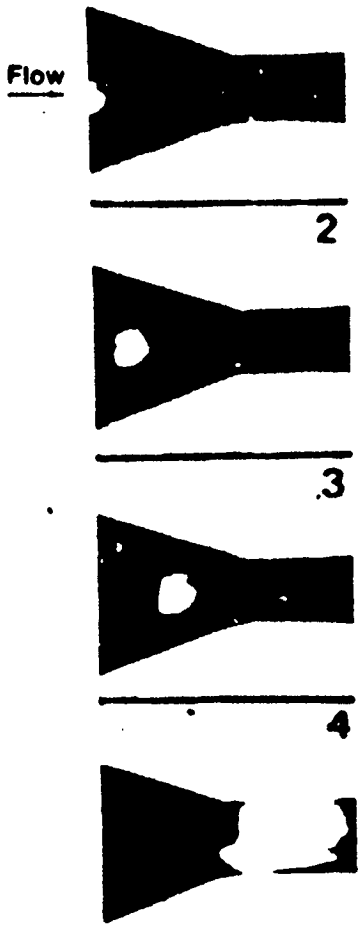

Figure 11 Agglomerates breaking up in nozzle.

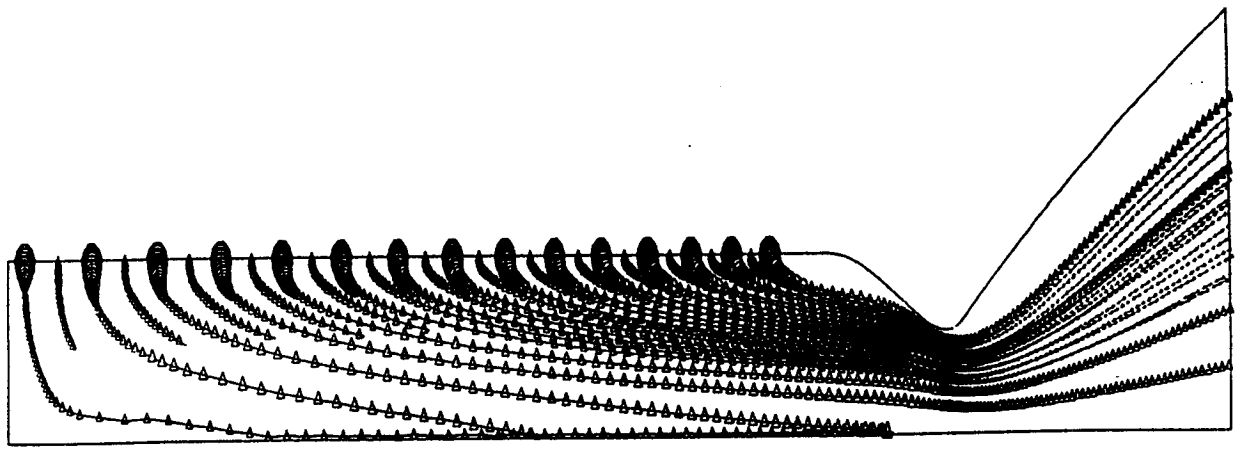

Figure 12 Particle trajectories with combustion/evaporation/breakup/agglomeration models.

Al particle (150μm)

Al_2O_3 particle (50μm)

XMIN=-7.71E+00
XMAX= 2.66E+00
YMIN=-3.56E+00
YMAX= 5.29E+00

Color-Map:

a	0.0000E+00
b	2.5869E-06
c	5.1739E-06
d	7.7609E-06
e	1.0347E-05
f	1.2934E-05
g	1.5521E-05
h	1.8108E-05
i	2.0695E-05
j	2.3282E-05
k	2.5869E-05
l	2.8456E-05
m	3.1043E-05
n	3.3630E-05
o	3.6217E-05
p	3.8804E-05
q	4.1391E-05
r	4.3978E-05
s	4.6565E-05
t	4.9152E-05
u	5.1739E-05
v	5.4326E-05
w	5.6913E-05
x	5.9500E-05
y	6.2087E-05
z	6.4674E-05

Figure 13 Mean particle size distributions of the 2D nozzle.

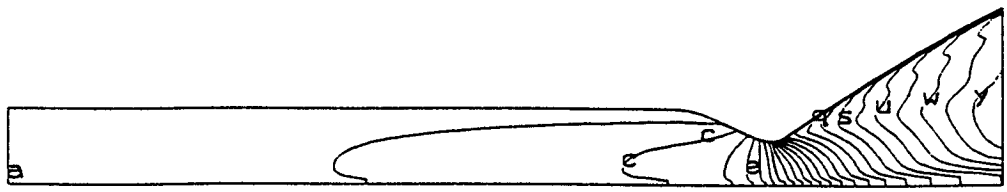

XMIN=-7.71E+00
XMAX= 2.66E+00
YMIN=-3.56E+00
YMAX= 5.29E+00

Color-Map:

a	0.0000E+00
b	1.3531E-01
c	2.7062E-01
d	4.0593E-01
e	5.4125E-01
f	6.7656E-01
g	8.1187E-01
h	9.4719E-01
i	1.0825E+00
j	1.2178E+00
k	1.3531E+00
l	1.4884E+00
m	1.6237E+00
n	1.7590E+00
o	1.8943E+00
p	2.0296E+00
q	2.1650E+00
r	2.3003E+00
s	2.4356E+00
t	2.5709E+00
u	2.7062E+00
v	2.8415E+00
w	2.9768E+00
x	3.1122E+00
y	3.2475E+00
z	3.3828E+00

Figure 14 Mach number contours of 2D nozzle, with chemical reaction and particles.

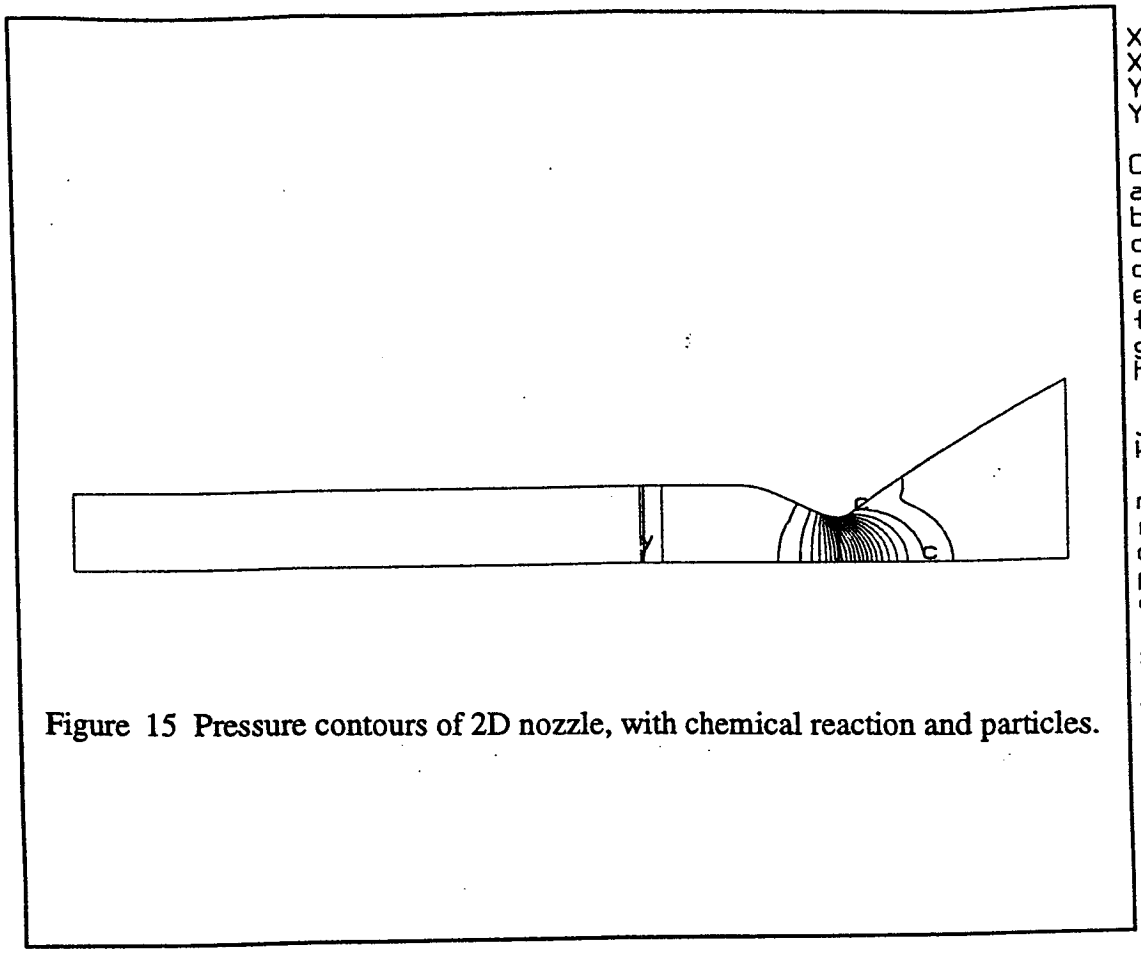

Figure 15 Pressure contours of 2D nozzle, with chemical reaction and particles.

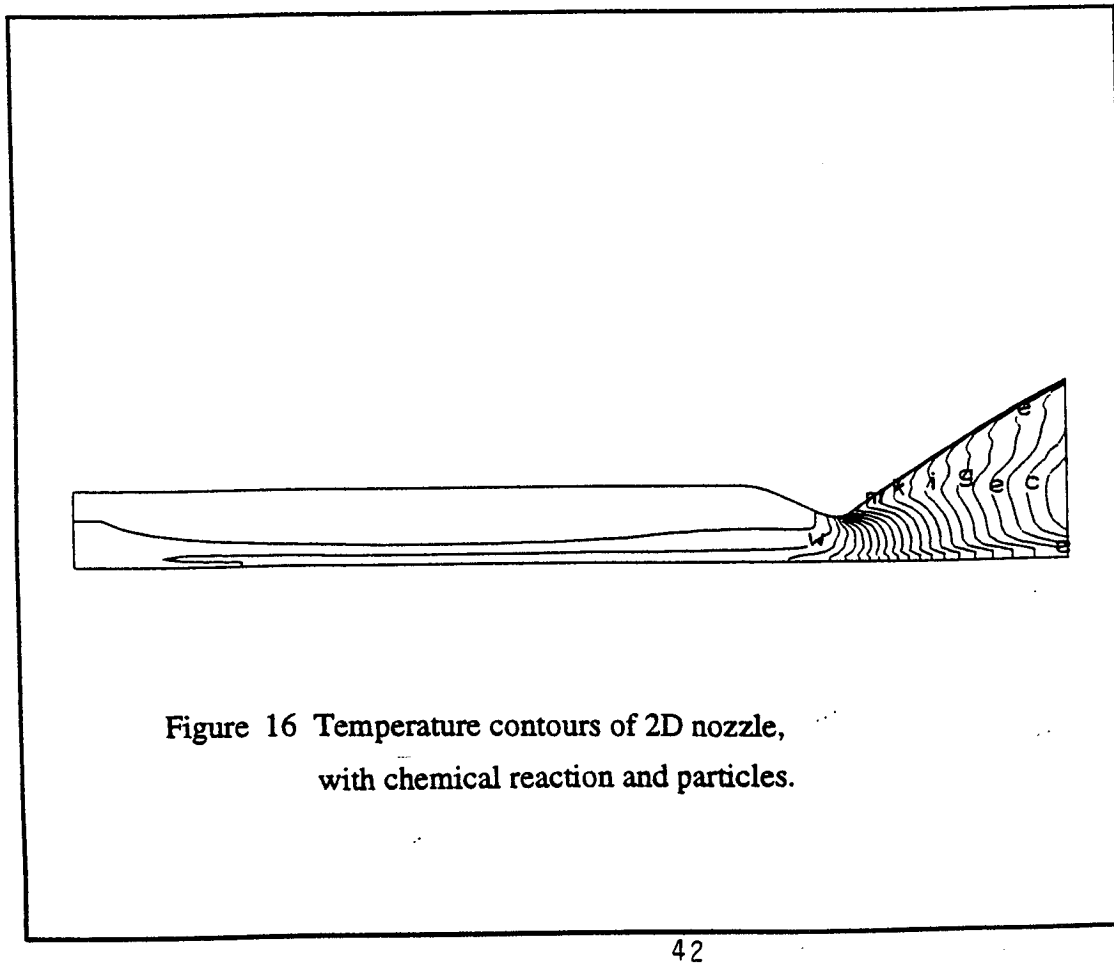

Figure 16 Temperature contours of 2D nozzle, with chemical reaction and particles.

THE ASRM

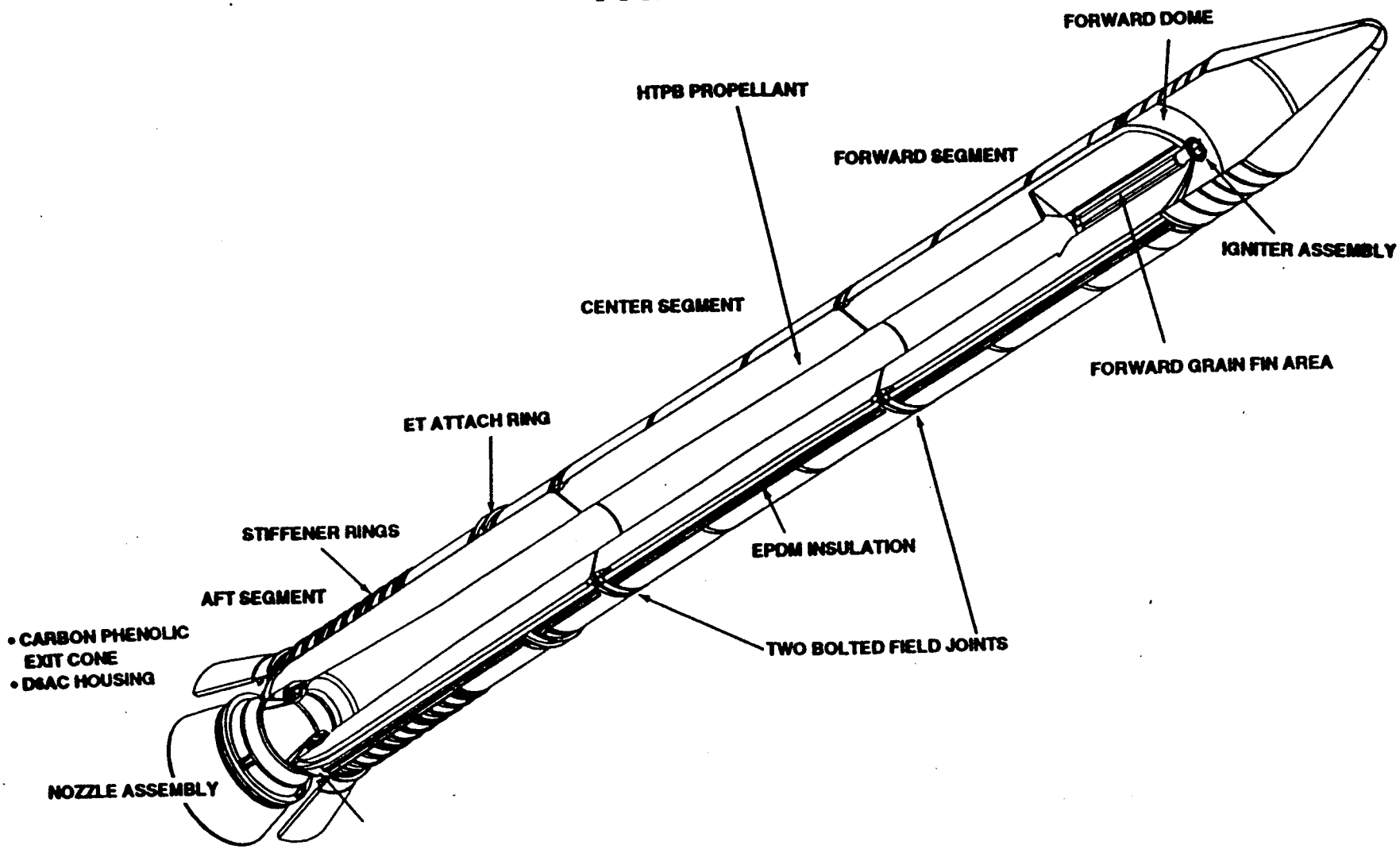

Figure 17 ASRM configuration.

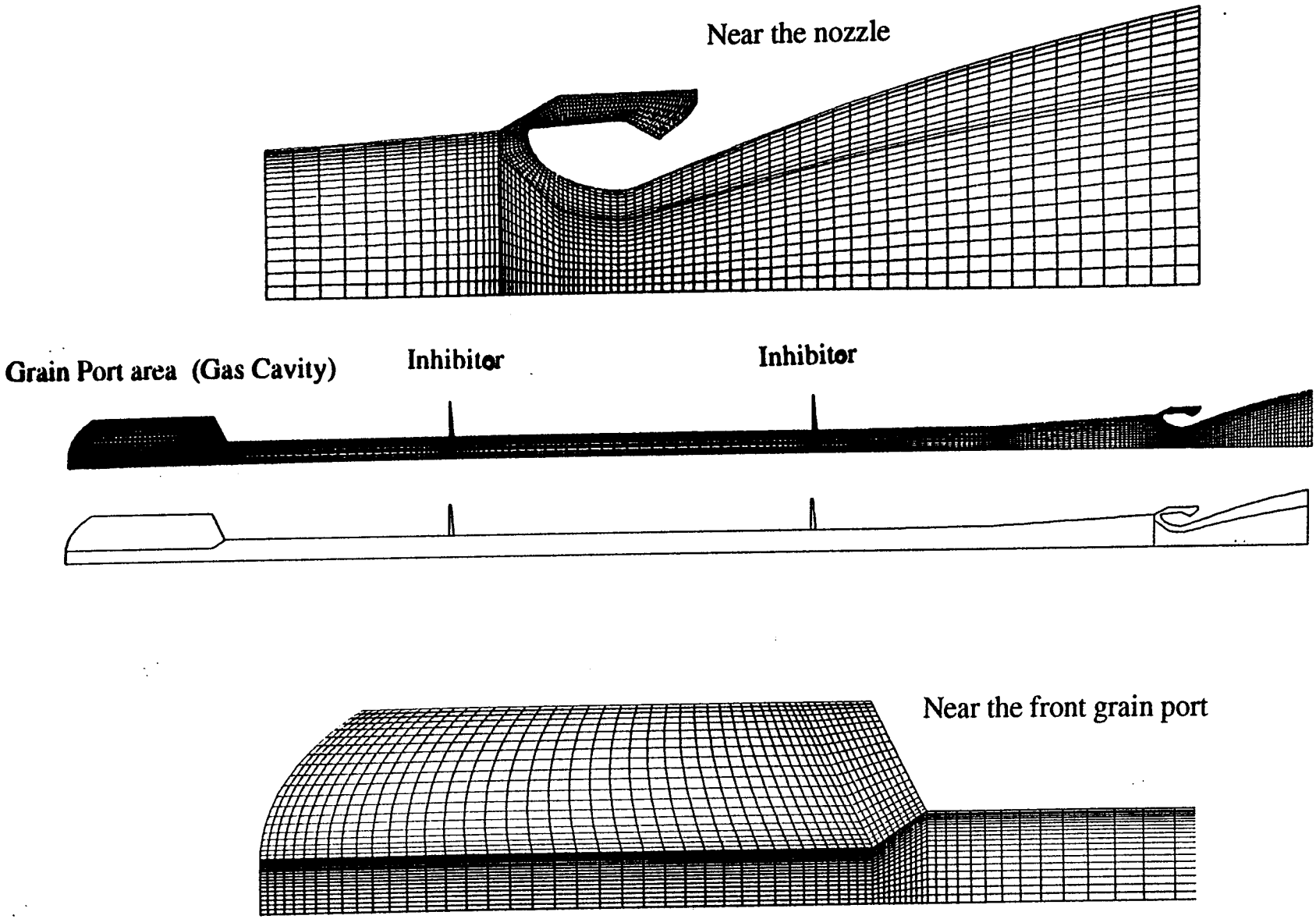

Figure 18 2D Grid system of the ASRM.

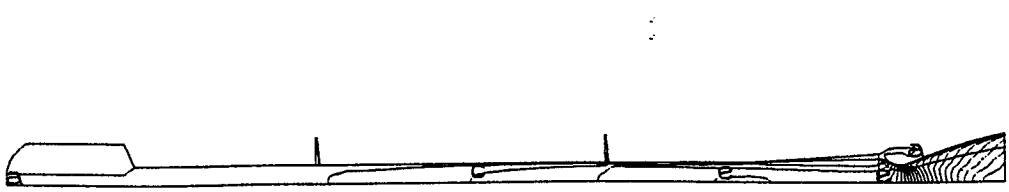

XMIN=-6.16E+00
XMAX= 1.33E+02
YMIN=-5.62E+01
YMAX= 6.24E+01

Color-Map
a 0.0000E+00
b 1.3622E-01
c 2.7244E-01
d 4.0866E-01
e 5.4488E-01
f 6.8110E-01
g 8.1732E-01
h 9.5354E-01
i 1.0897E+00
j 1.2259E+00
k 1.3622E+00
l 1.4984E+00
m 1.6346E+00
n 1.7708E+00
o 1.9070E+00
p 2.0433E+00
q 2.1795E+00
r 2.3157E+00
s 2.4519E+00
t 2.5882E+00
u 2.7244E+00
v 2.8606E+00
w 2.9968E+00
x 3.1330E+00
y 3.2693E+00
z 3.4055E+00

Figure 19 Mach number contours of 2D ASRM, no chemical reaction, no particles.

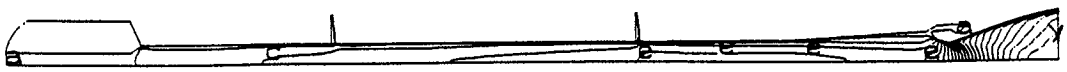

XMIN=-2.50E+00
XMAX= 1.29E+02
YMIN=-5.31E+01
YMAX= 5.93E+01

Color-Map
a 0.0000E+00
b 1.2630E-01
c 2.5261E-01
d 3.7892E-01
e 5.0522E-01
f 6.3153E-01
g 7.5784E-01
h 8.8415E-01
i 1.0104E+00
j 1.1367E+00
k 1.2630E+00
l 1.3893E+00
m 1.5156E+00
n 1.6419E+00
o 1.7683E+00
p 1.8946E+00
q 2.0209E+00
r 2.1472E+00
s 2.2735E+00
t 2.3998E+00
u 2.5261E+00
v 2.6524E+00
w 2.7787E+00
x 2.9050E+00
y 3.0313E+00
z 3.1576E+00

Figure 20 Mach number contours of 2D ASRM, with chemical reaction, no particles.

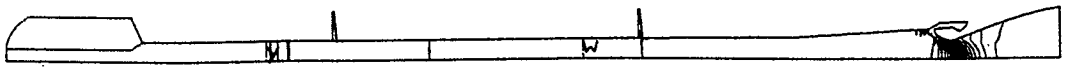

XMIN=-2.50E+00
XMAX= 1.29E+02
YMIN=-5.31E+01
YMAX= 5.93E+01

Color-Map:

a	1.2259E+01
b	4.8740E+01
c	8.5223E+01
d	1.2170E+02
e	1.5818E+02
f	1.9467E+02
g	2.3115E+02
h	2.6763E+02
i	3.0411E+02
j	3.4060E+02
k	3.7708E+02
l	4.1356E+02
m	4.5004E+02
n	4.8653E+02
o	5.2301E+02
p	5.5949E+02
q	5.9597E+02
r	6.3246E+02
s	6.6894E+02
t	7.0542E+02
u	7.4190E+02
v	7.7839E+02
w	8.1487E+02
x	8.5135E+02
y	8.8783E+02
z	9.2432E+02

Figure 21 Pressure contours of 2D ASRM, with chemical reaction, no particles.

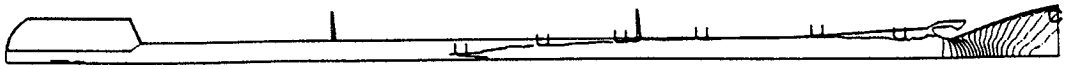

XMIN=-2.50E+00
XMAX= 1.29E+02
YMIN=-5.31E+01
YMAX= 5.93E+01

Color-Map:

a	3.0969E+03
b	3.2256E+03
c	3.3543E+03
d	3.4830E+03
e	3.6117E+03
f	3.7404E+03
g	3.8691E+03
h	3.9978E+03
i	4.1265E+03
j	4.2552E+03
k	4.3839E+03
l	4.5126E+03
m	4.6413E+03
n	4.7700E+03
o	4.8987E+03
p	5.0274E+03
q	5.1561E+03
r	5.2848E+03
s	5.4135E+03
t	5.5422E+03
u	5.6709E+03
v	5.7996E+03
w	5.9283E+03
x	6.0570E+03
y	6.1857E+03
z	6.3144E+03

Figure 22 Temperature contours of 2D ASRM, with chemical reaction, no particles.

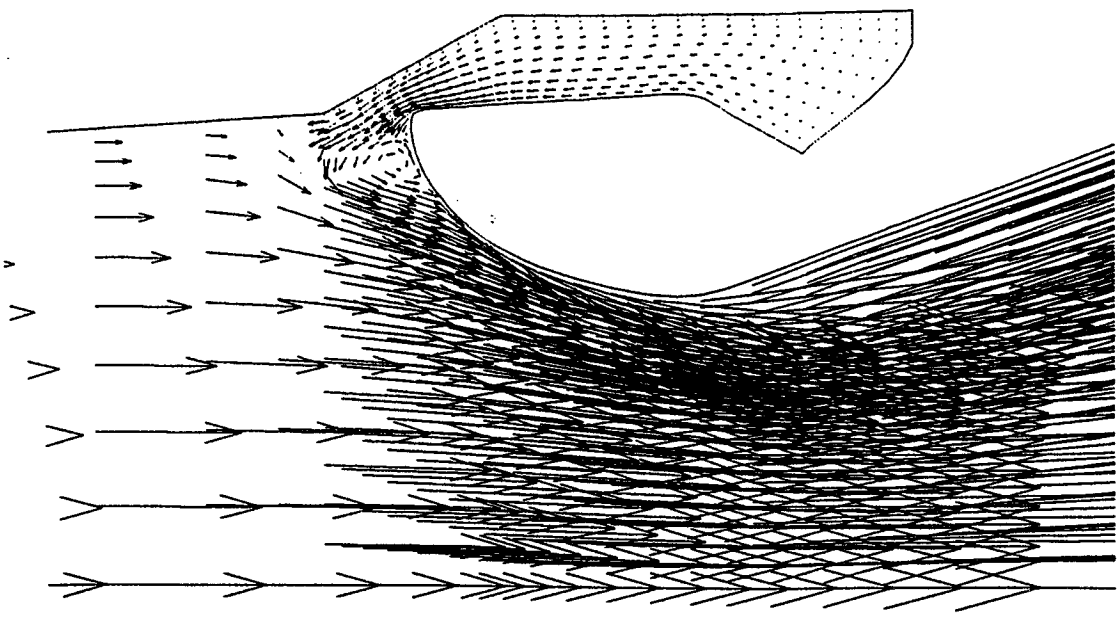

Figure 23 Velocity vectors of the 2D ASRM, with chemical reaction, no particles.

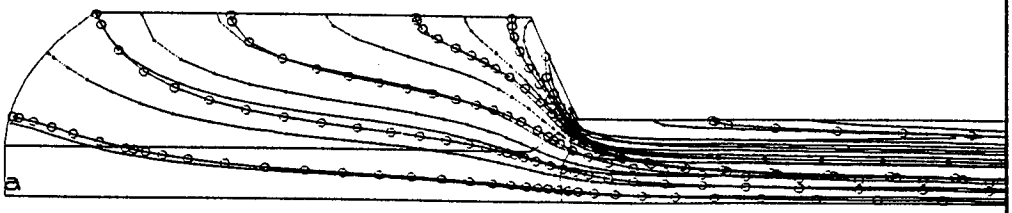

Figure 24 Particle trajectories near the front grain portion.

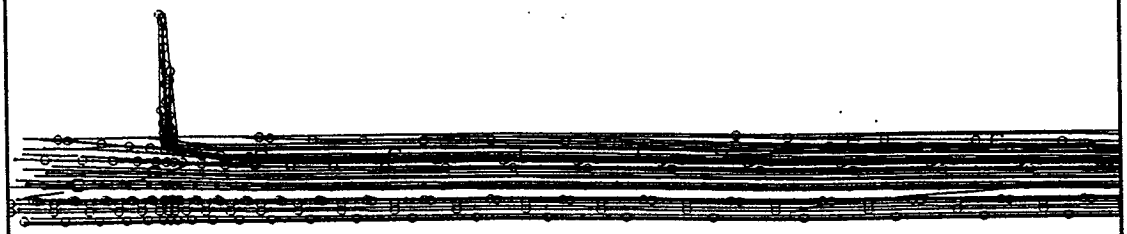

Figure 25 Particle trajectories near the first inhibitor.

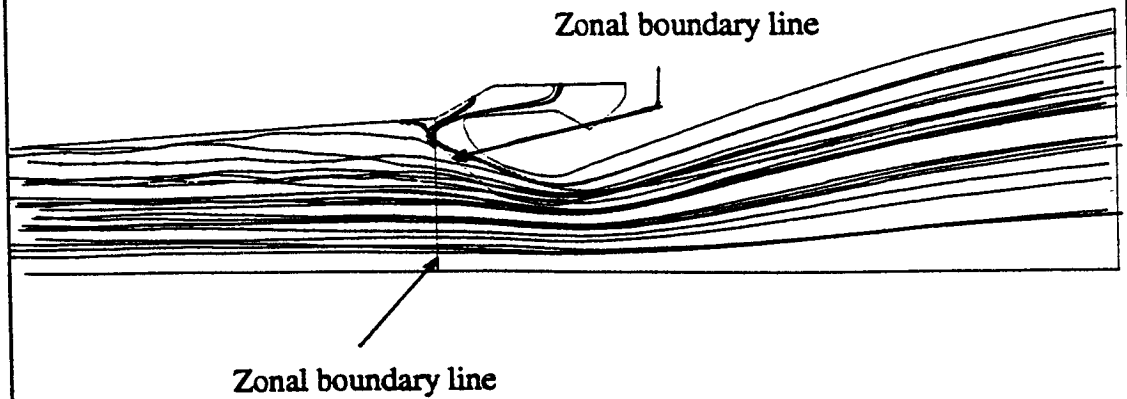

Figure 26 Particle trajectories near the nozzle.

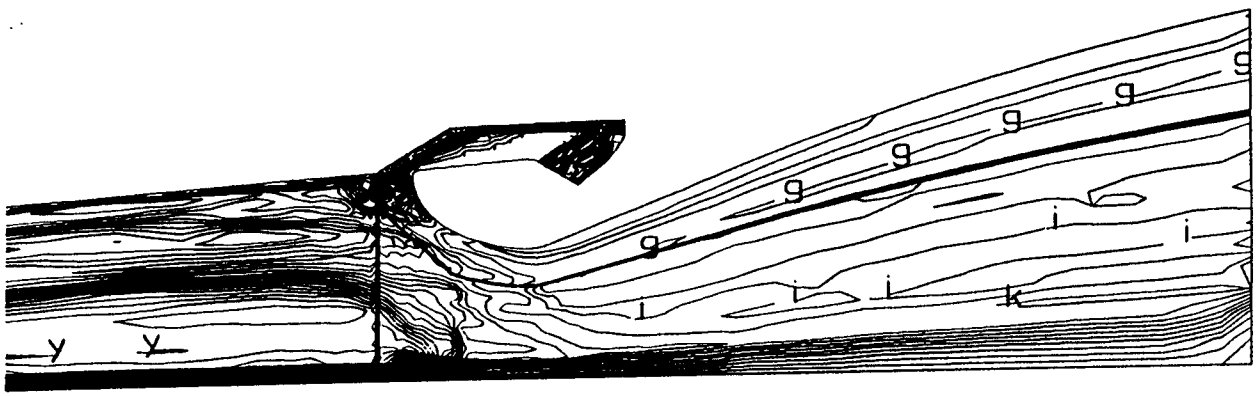

XMIN= 1.03E+02
XMAX= 1.28E+02
YMIN=-7.80E+00
YMAX= 1.40E+01

Color-Map:

a	0.0000E+00
b	2.0000E-06
c	4.0000E-06
d	6.0000E-06
e	8.0000E-06
f	1.0000E-05
g	1.2000E-05
h	1.3999E-05
i	1.5999E-05
j	1.8000E-05
k	1.9999E-05
l	2.2000E-05
m	2.4000E-05
n	2.5999E-05
o	2.7999E-05
p	2.9999E-05
q	3.1999E-05
r	3.4000E-05
s	3.6000E-05
t	3.7999E-05
u	3.9999E-05
v	4.1999E-05
w	4.4000E-05
x	4.5999E-05
y	4.8000E-05
z	5.0000E-05

Figure 27 Mean particle size distributions near the nozzle.

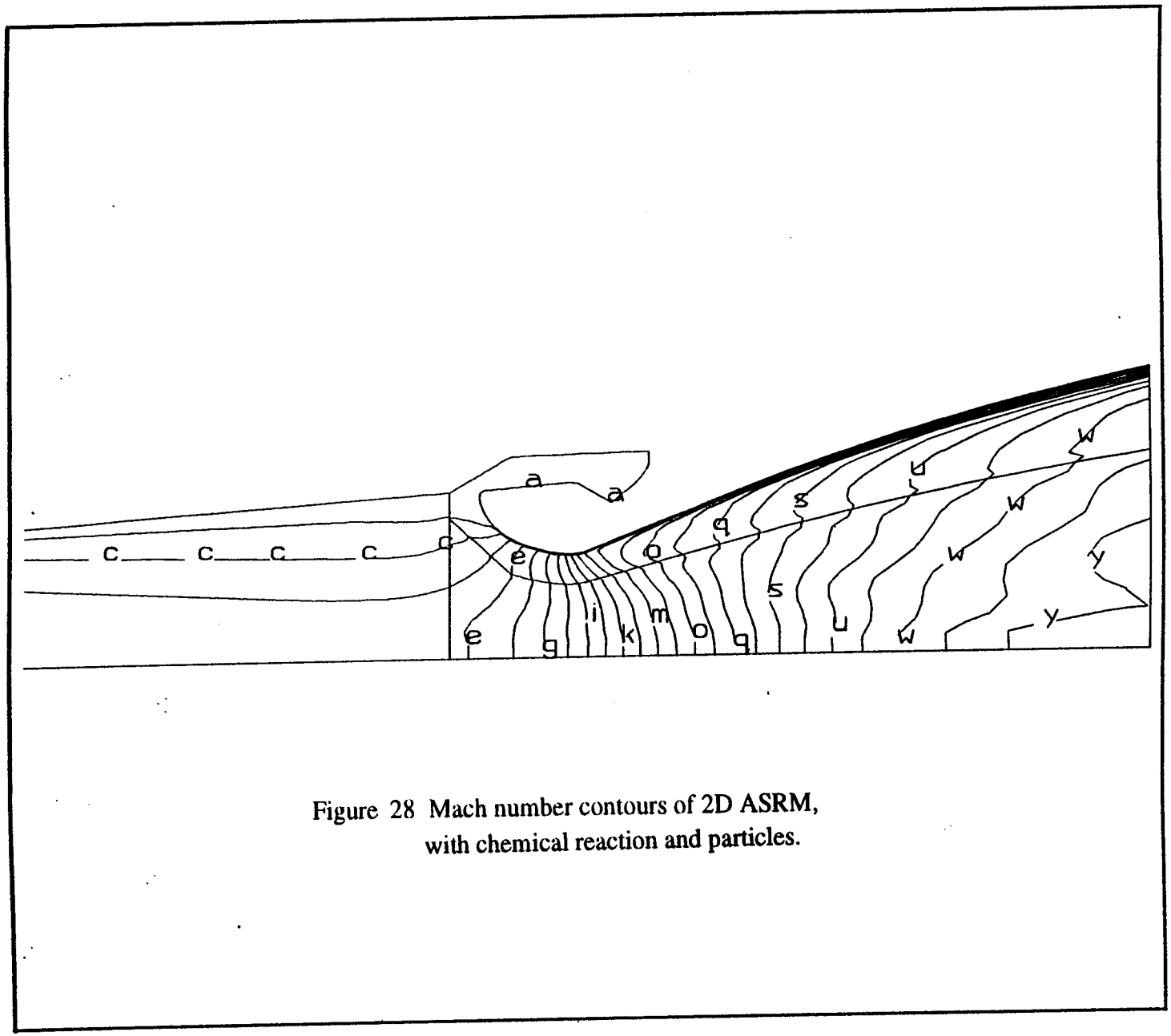

Figure 28 Mach number contours of 2D ASRM, with chemical reaction and particles.

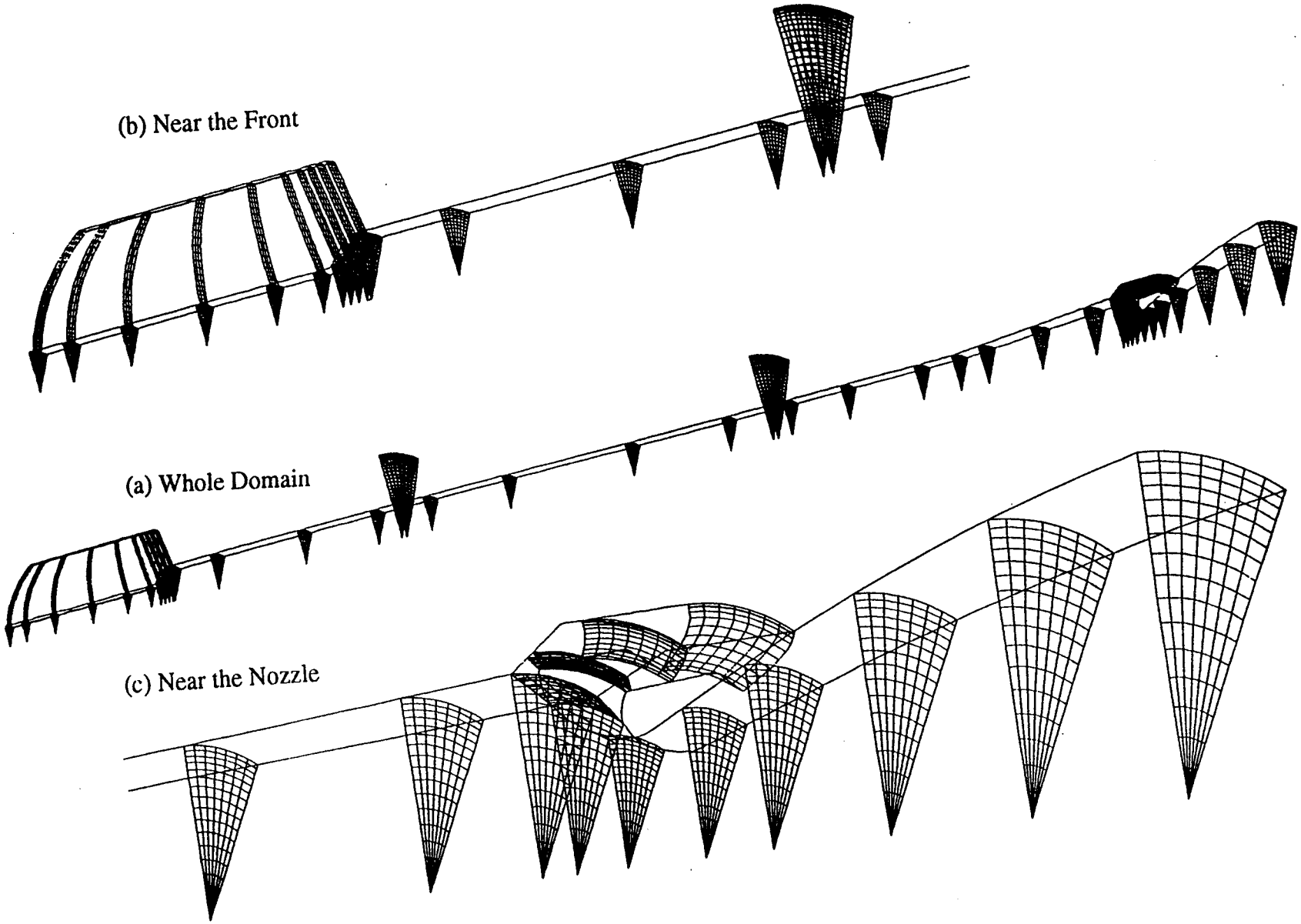

Figure 29 3D Grid system of ASRM.

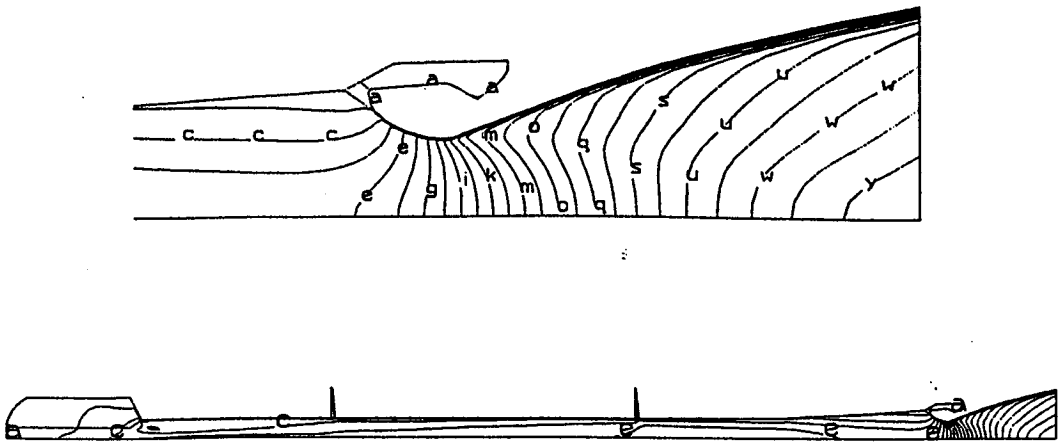

a	0.0000E+00
b	1.4035E-01
c	2.8071E-01
d	4.2107E-01
e	5.6143E-01
f	7.0178E-01
g	8.4214E-01
h	9.8250E-01
i	1.1228E+00
j	1.2632E+00
k	1.4035E+00
l	1.5439E+00
m	1.6842E+00
n	1.8246E+00
o	1.9650E+00
p	2.1053E+00
q	2.2457E+00
r	2.3860E+00
s	2.5264E+00
t	2.6667E+00
u	2.8071E+00
v	2.9475E+00
w	3.0878E+00
x	3.2282E+00
y	3.3685E+00
z	3.5089E+00

Figure 30 Mach number contours of 3D ASRM, with chemical reaction, no particles.

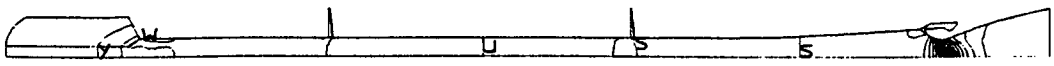

XMIN=-2.50E+00
XMAX= 1.29E+02
YMIN=-5.31E+01
YMAX= 5.93E+01

Color-Map

a	1.0099E+01
b	6.0801E+01
c	1.1150E+02
d	1.6220E+02
e	2.1290E+02
f	2.6360E+02
g	3.1430E+02
h	3.6501E+02
i	4.1571E+02
j	4.6641E+02
k	5.1711E+02
l	5.6781E+02
m	6.1852E+02
n	6.6922E+02
o	7.1992E+02
p	7.7062E+02
q	8.2132E+02
r	8.7202E+02
s	9.2273E+02
t	9.7343E+02
u	1.0241E+03
v	1.0748E+03
w	1.1255E+03
x	1.1762E+03
y	1.2269E+03
z	1.2776E+03

Figure 31 Pressure contours of 3D ASRM, with chemical reaction, no particles.

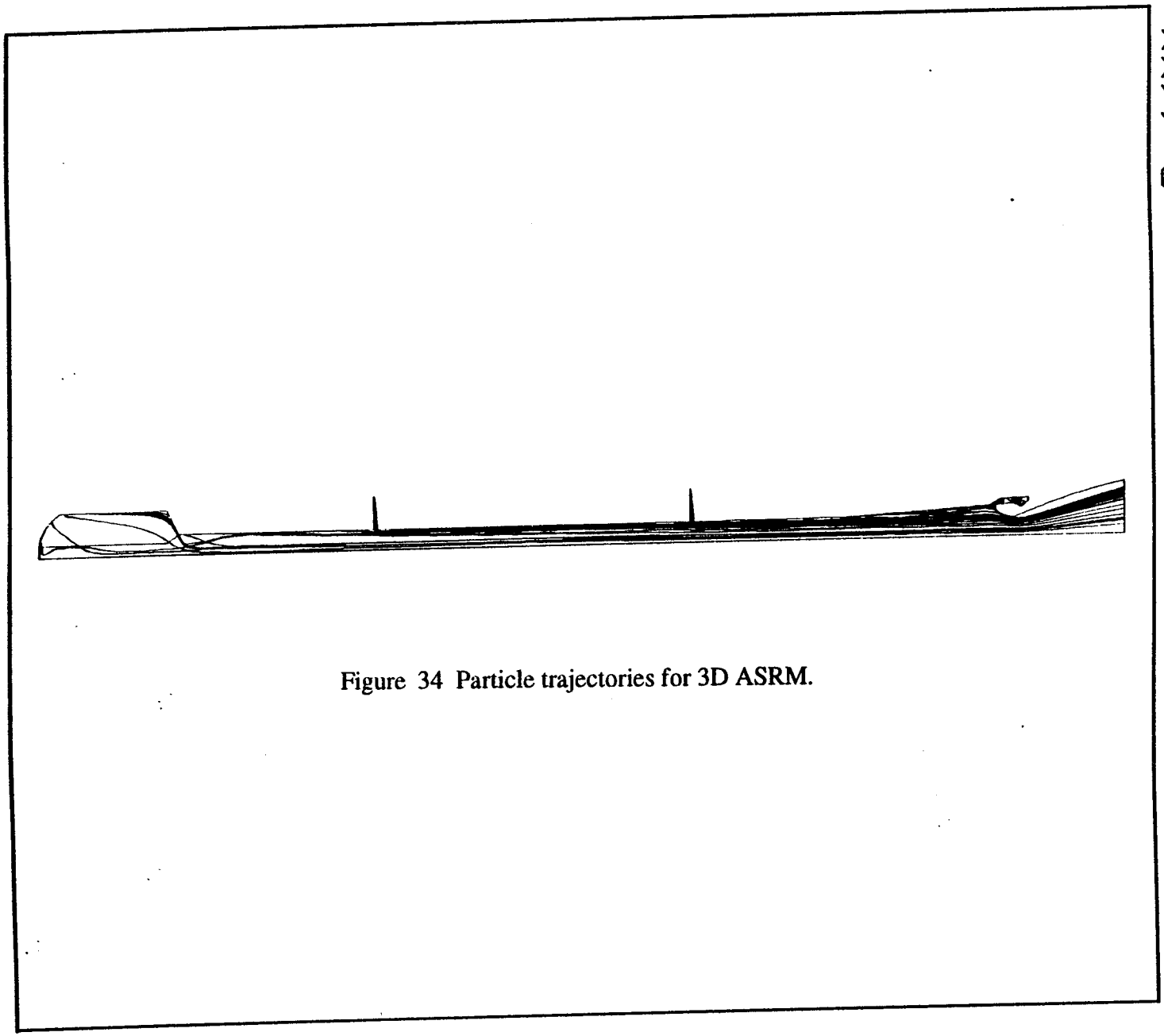

Figure 34 Particle trajectories for 3D ASRM.

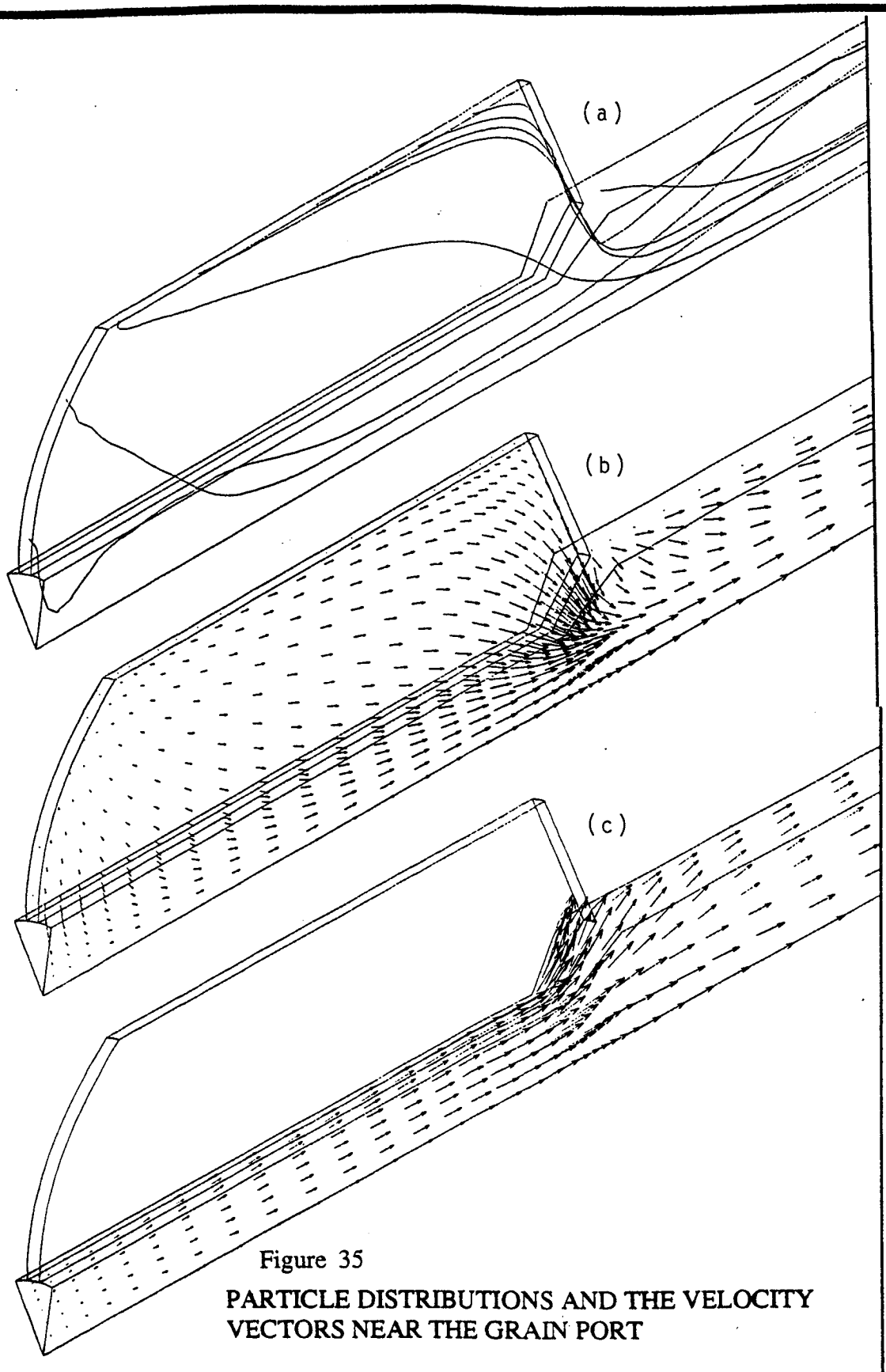

Figure 35

PARTICLE DISTRIBUTIONS AND THE VELOCITY VECTORS NEAR THE GRAIN PORT

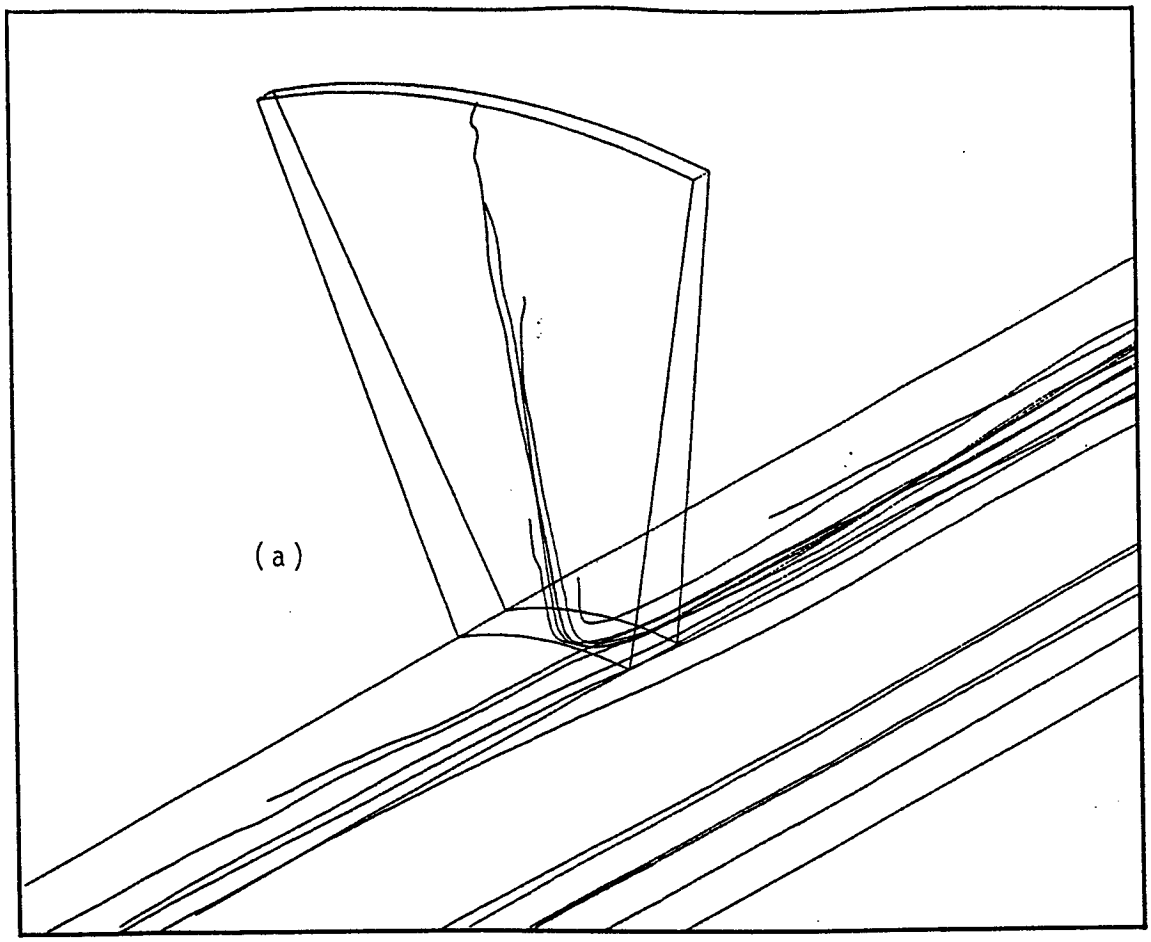

Figure 36 Particle trajectories and velocity vectors near the first inhibitor.

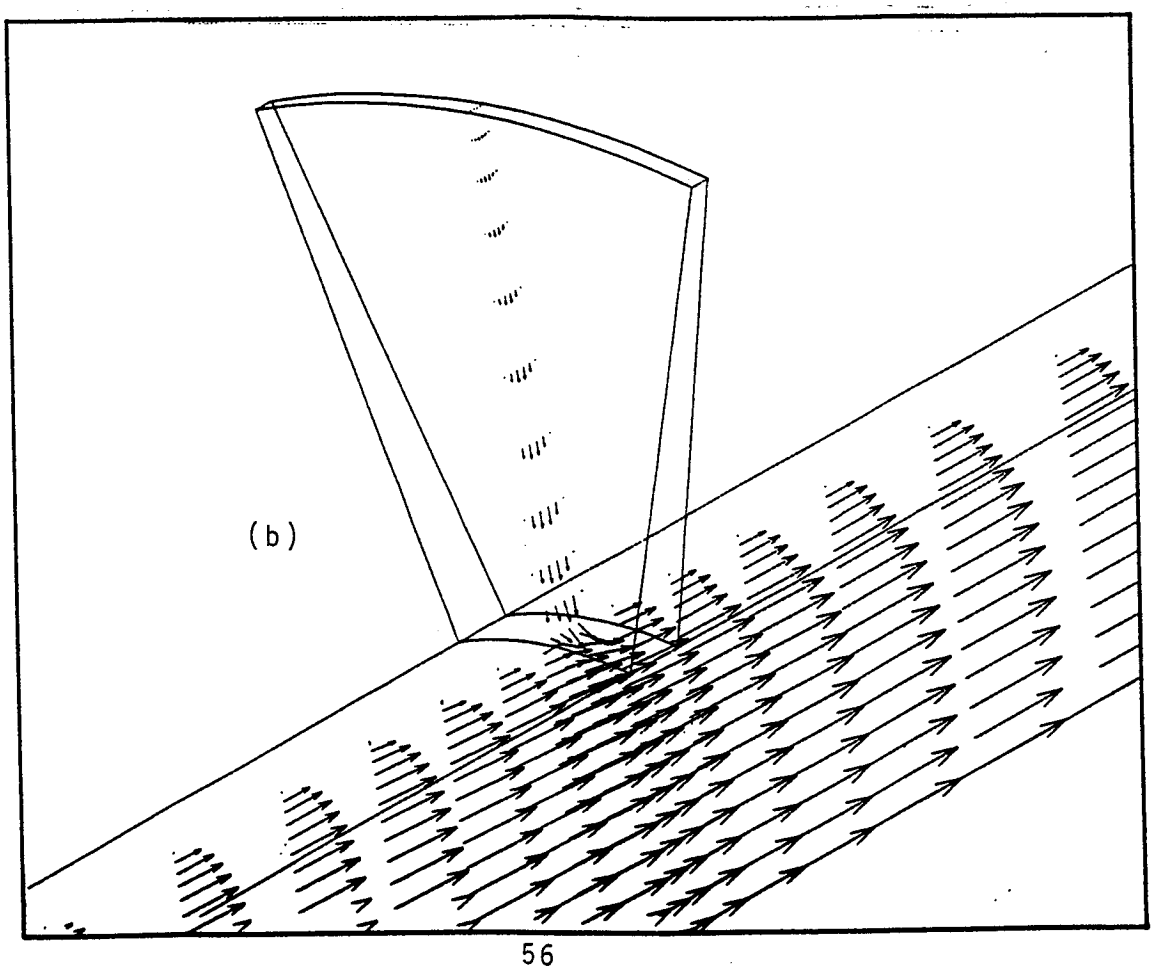

Figure 37 Particle trajectories and velocity vectors near the aft-end cavity.

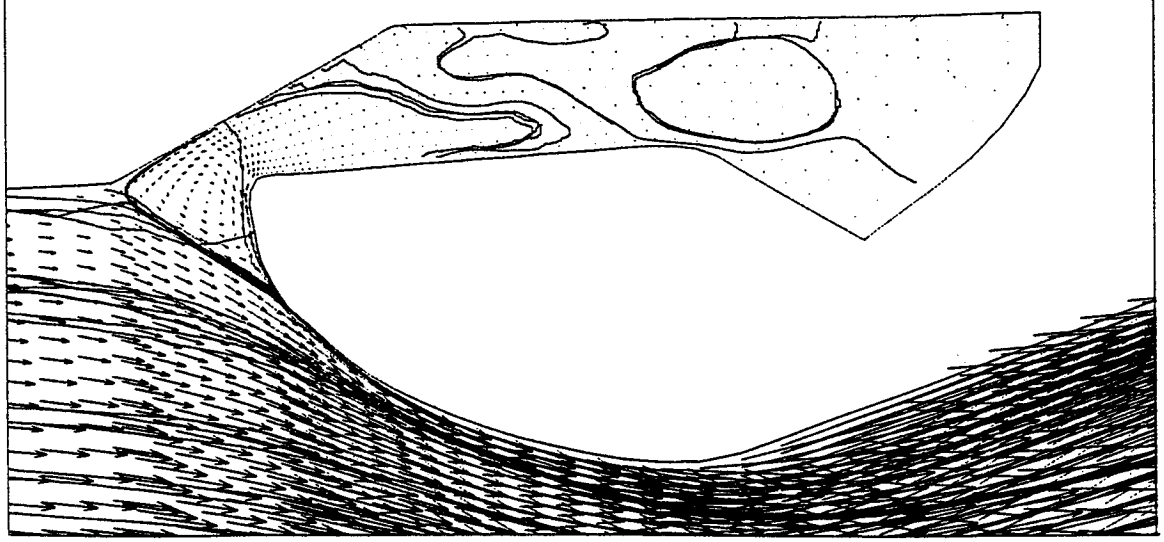

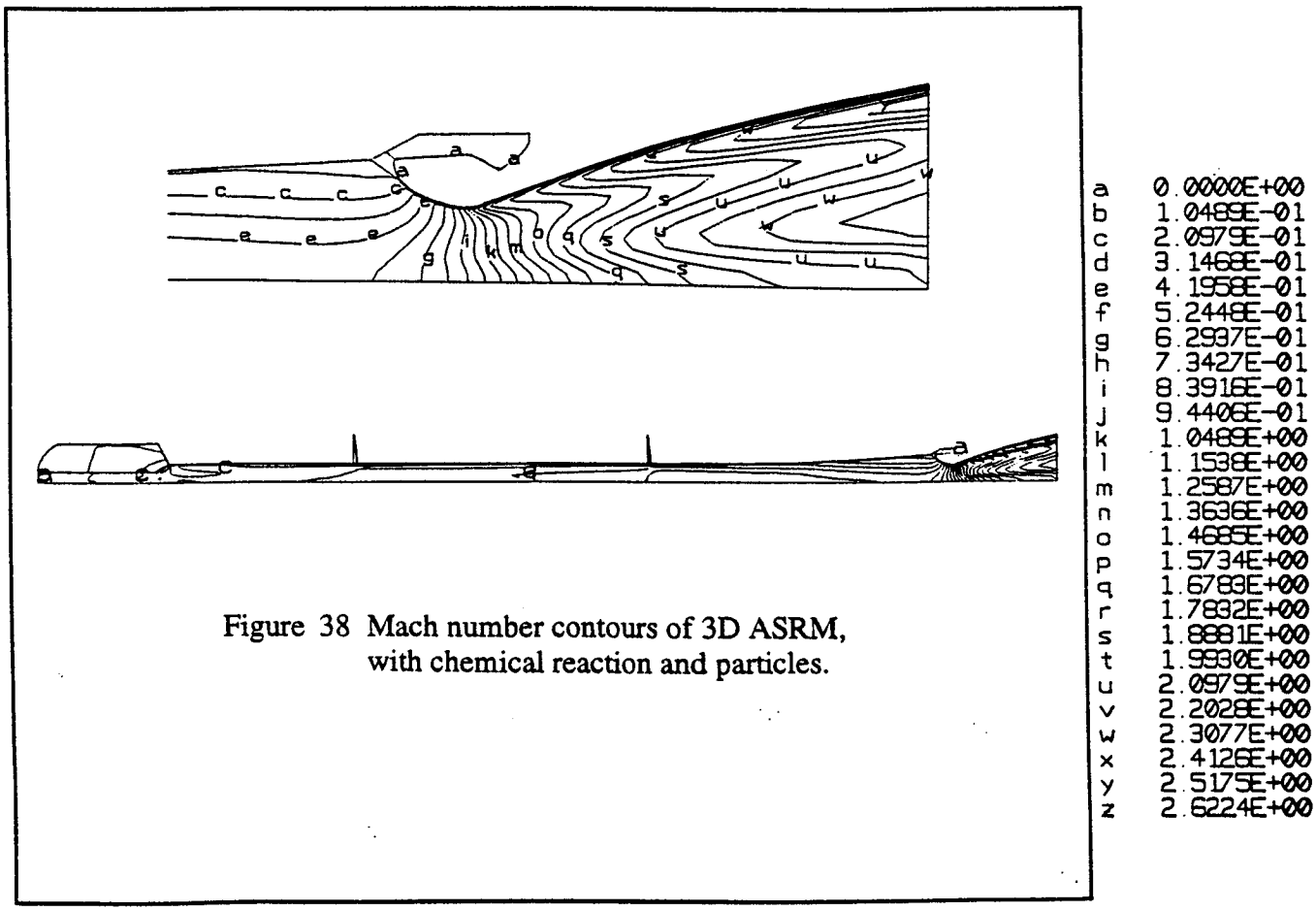

Figure 38 Mach number contours of 3D ASRM, with chemical reaction and particles.

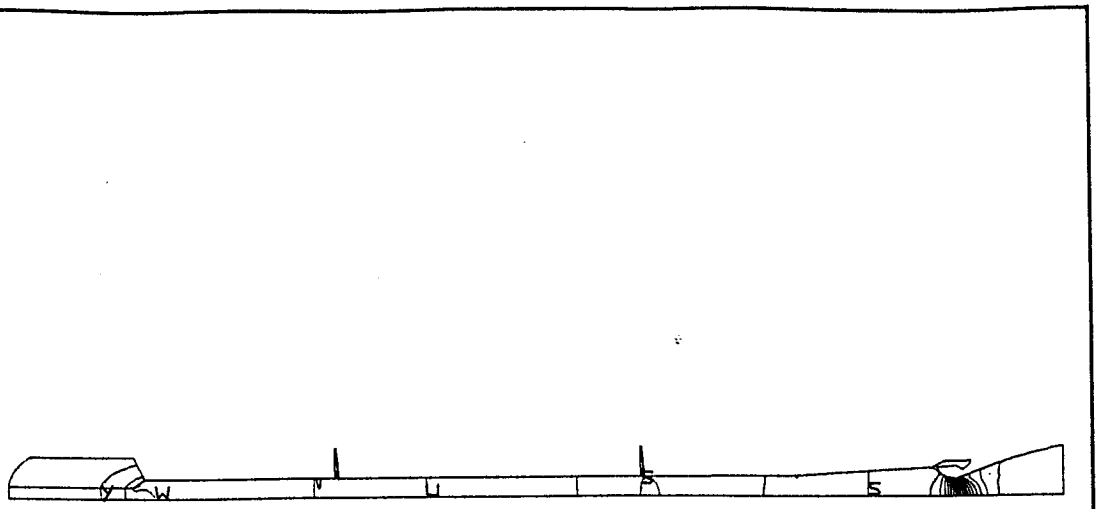

XMIN=-2.50E+00
XMAX= 1.29E+02
YMIN=-5.31E+01
YMAX= 5.93E+01

Color-Map

a	2.0144E+01
b	7.4225E+01
c	1.2830E+02
d	1.8238E+02
e	2.3646E+02
f	2.9054E+02
g	3.4463E+02
h	3.9871E+02
i	4.5279E+02
j	5.0687E+02
k	5.6095E+02
l	6.1503E+02
m	6.6911E+02
n	7.2319E+02
o	7.7728E+02
p	8.3136E+02
q	8.8544E+02
r	9.3952E+02
s	9.9360E+02
t	1.0476E+03
u	1.1017E+03
v	1.1558E+03
w	1.2099E+03
x	1.2640E+03
y	1.3180E+03
z	1.3721E+03

Figure 39 Pressure contours of 3D ASRM, with chemical reaction and particles.

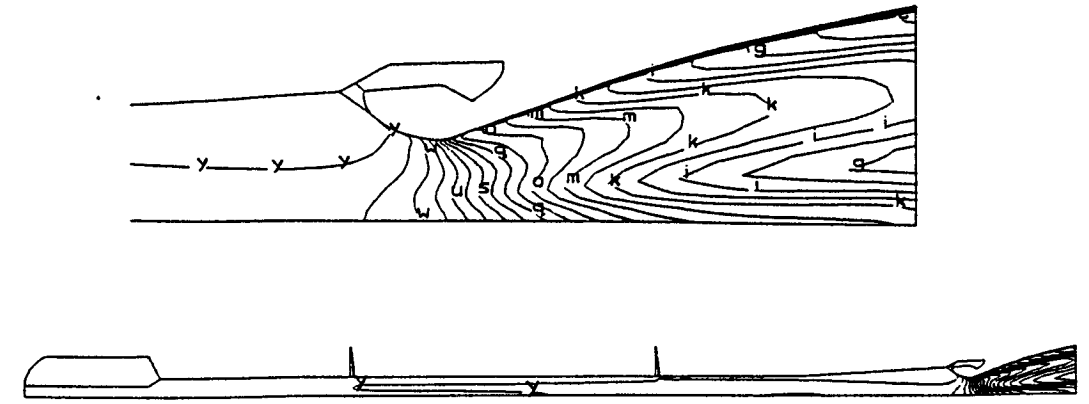

a	2.6455E+03
b	2.7924E+03
c	2.9394E+03
d	3.0863E+03
e	3.2332E+03
f	3.3802E+03
g	3.5271E+03
h	3.6740E+03
i	3.8210E+03
j	3.9679E+03
k	4.1148E+03
l	4.2618E+03
m	4.4087E+03
n	4.5556E+03
o	4.7026E+03
p	4.8495E+03
q	4.9964E+03
r	5.1434E+03
s	5.2903E+03
t	5.4372E+03
u	5.5842E+03
v	5.7311E+03
w	5.8781E+03
x	6.0250E+03
y	6.1719E+03
z	6.3189E+03

Figure 40 Temperature contours of 3D ASRM, with chemical reaction and particles.

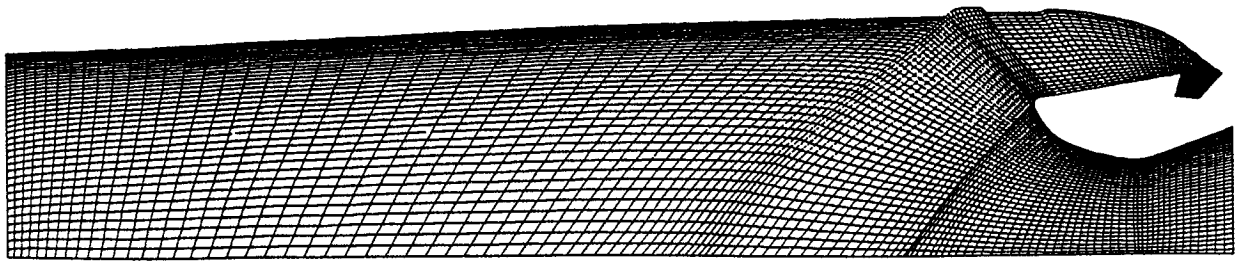

Figure 41 2D Grid system of RSRM configuration.

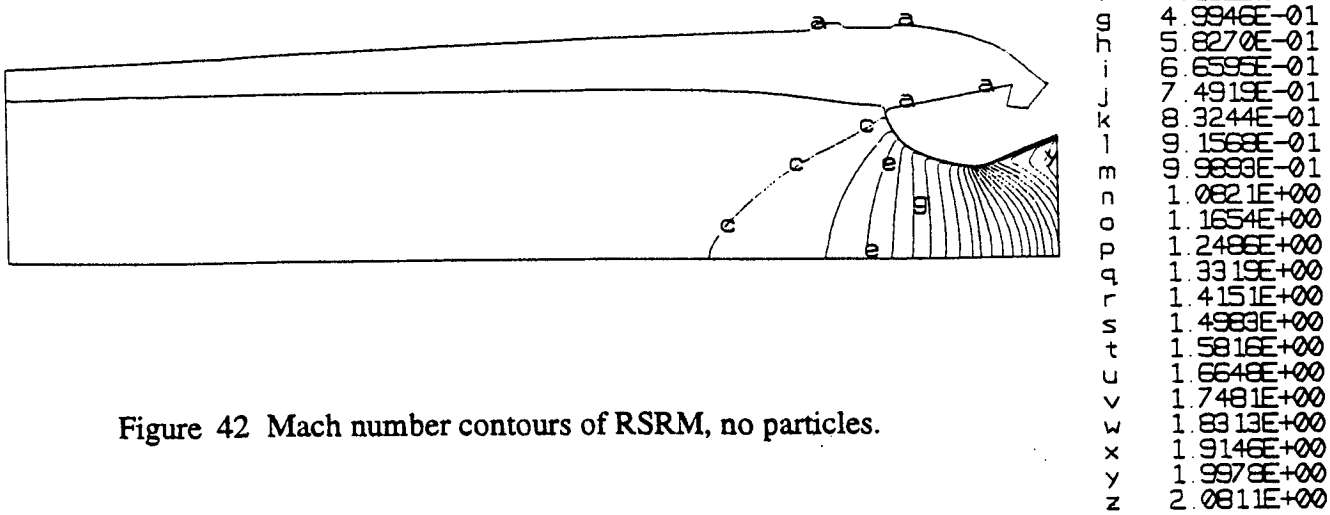

Figure 42 Mach number contours of RSRM, no particles.

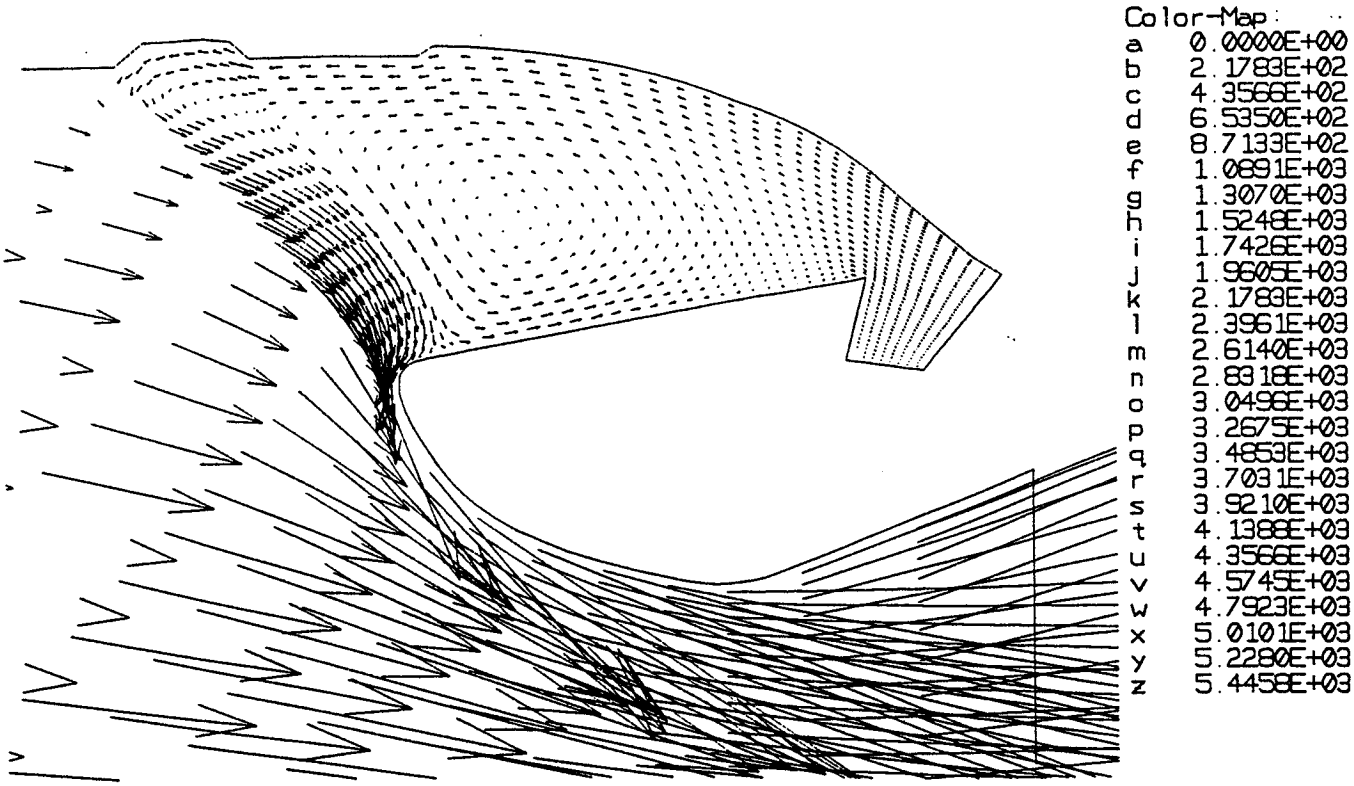

Figure 45 Velocity vectors near the aft-end cavity, no particles.

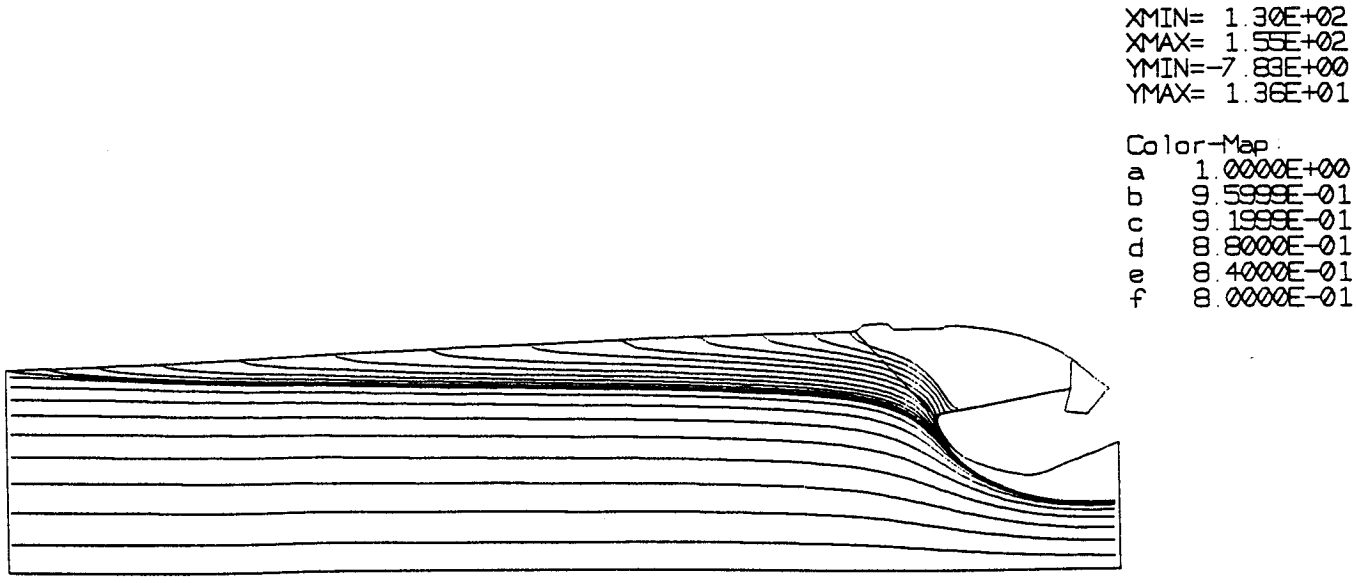

Figure 46 Particle trajectories.

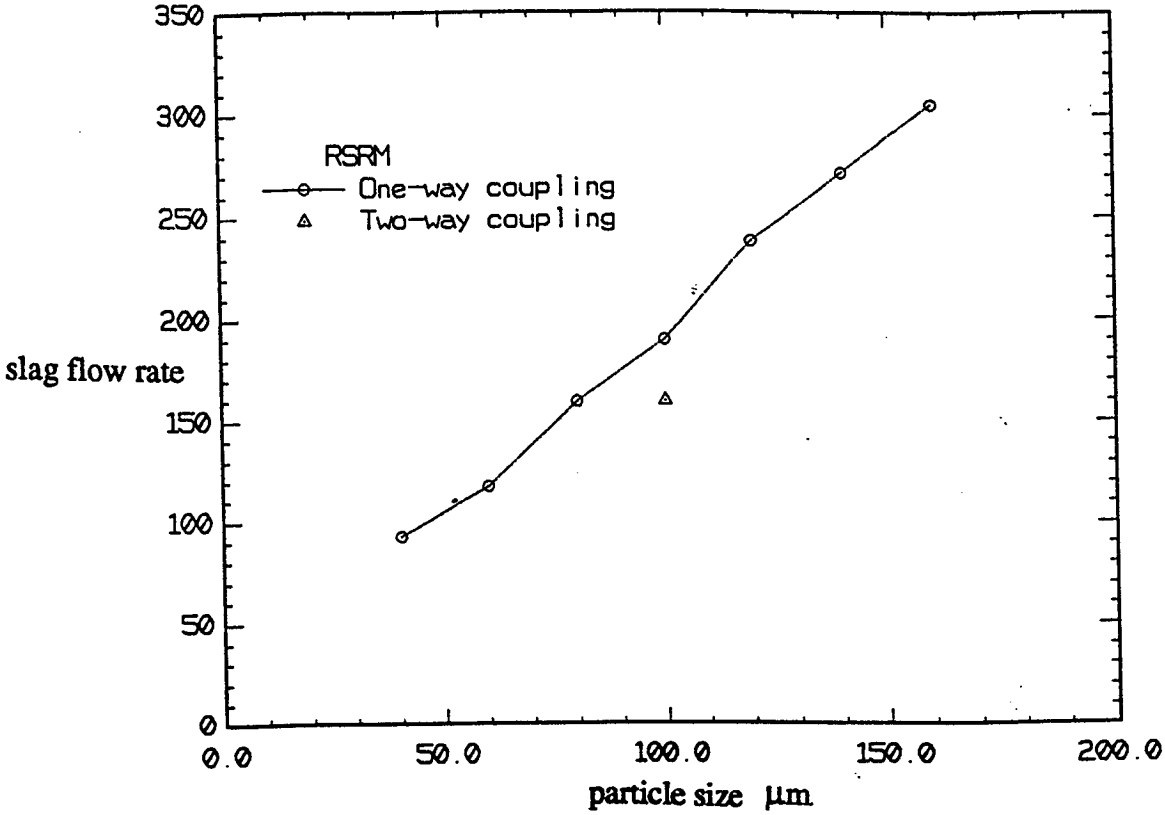

Figure 47 Slag flow rate entering the aft-end cavity v.s. particle sizes.

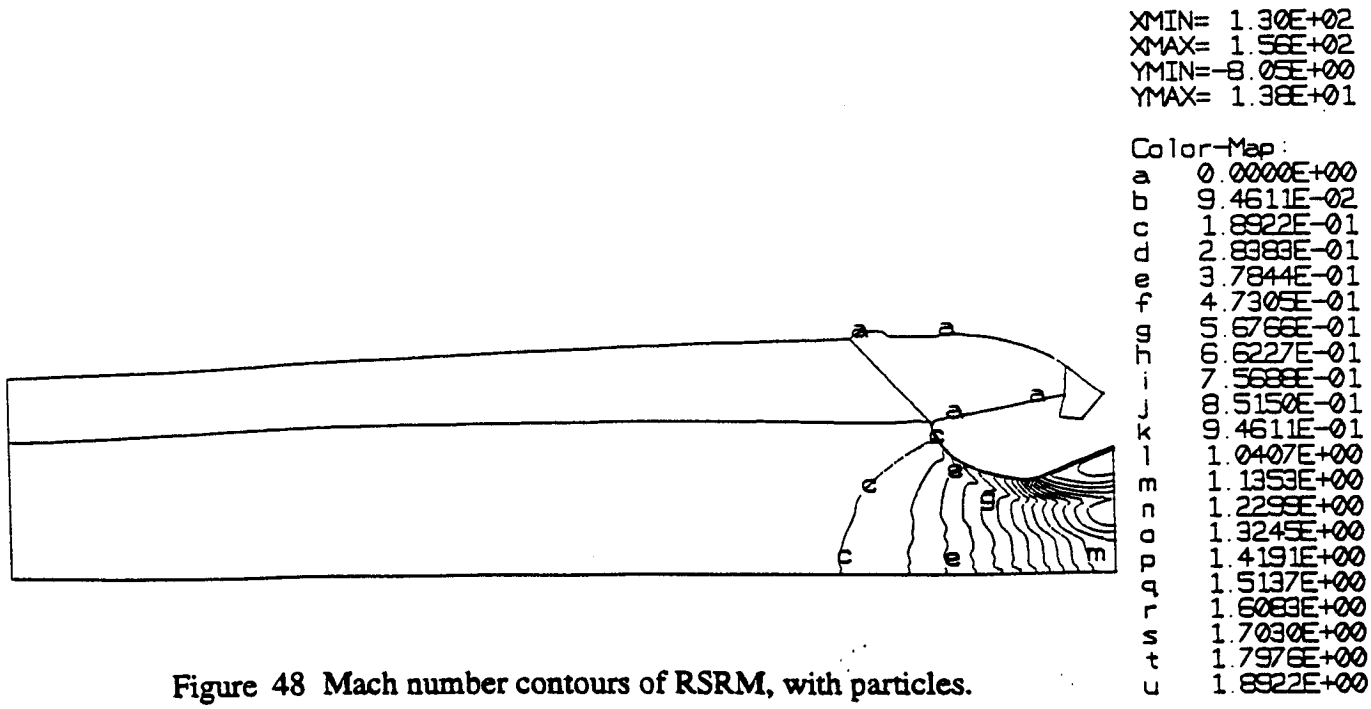

Figure 48 Mach number contours of RSRM, with particles.

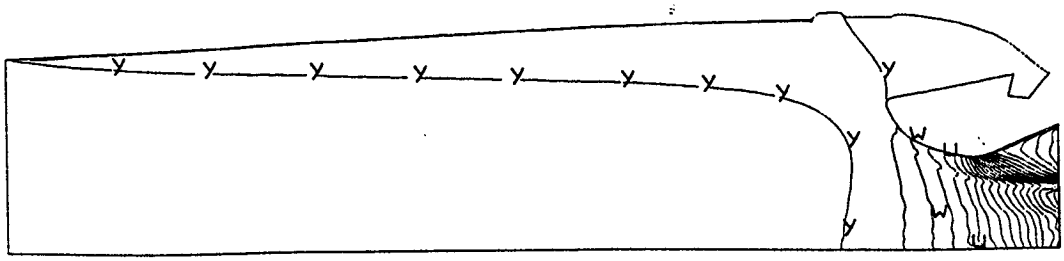

XMIN= 1.29E+02
XMAX= 1.56E+02
YMIN=-8.40E+00
YMAX= 1.42E+01

Color-Map

a	4.1296E+03
b	4.2099E+03
c	4.2902E+03
d	4.3705E+03
e	4.4508E+03
f	4.5310E+03
g	4.6113E+03
h	4.6916E+03
i	4.7719E+03
j	4.8522E+03
k	4.9325E+03
l	5.0128E+03
m	5.0930E+03
n	5.1733E+03
o	5.2536E+03
p	5.3339E+03
q	5.4142E+03
r	5.4945E+03
s	5.5747E+03
t	5.6550E+03
u	5.7353E+03
v	5.8156E+03
w	5.8959E+03
x	5.9762E+03
y	6.0565E+03
z	6.1367E+03

Figure 49 Temperature contours of RSRM, with particles.

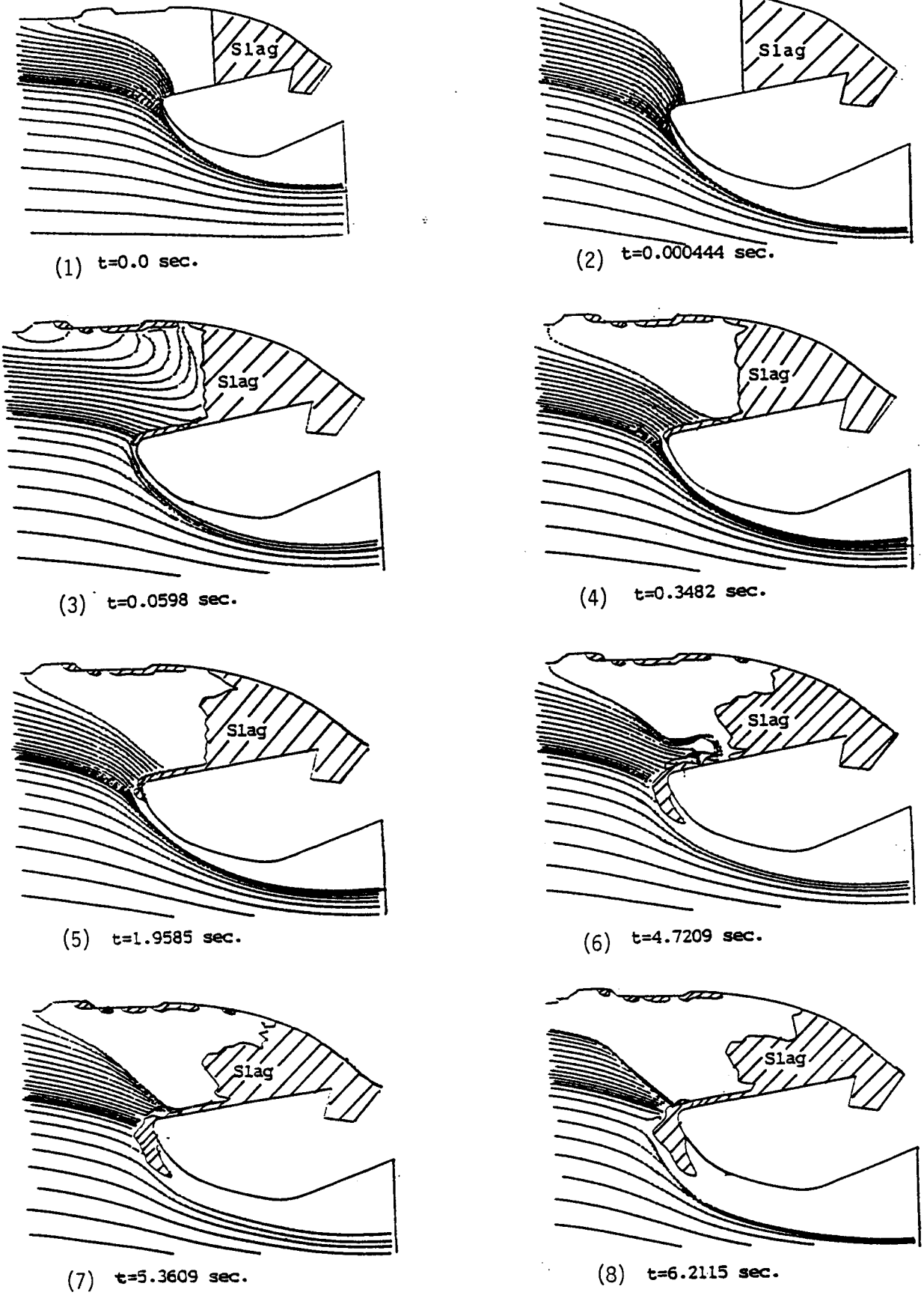

Figure 50 Slag buildup history in the aft-end cavity.

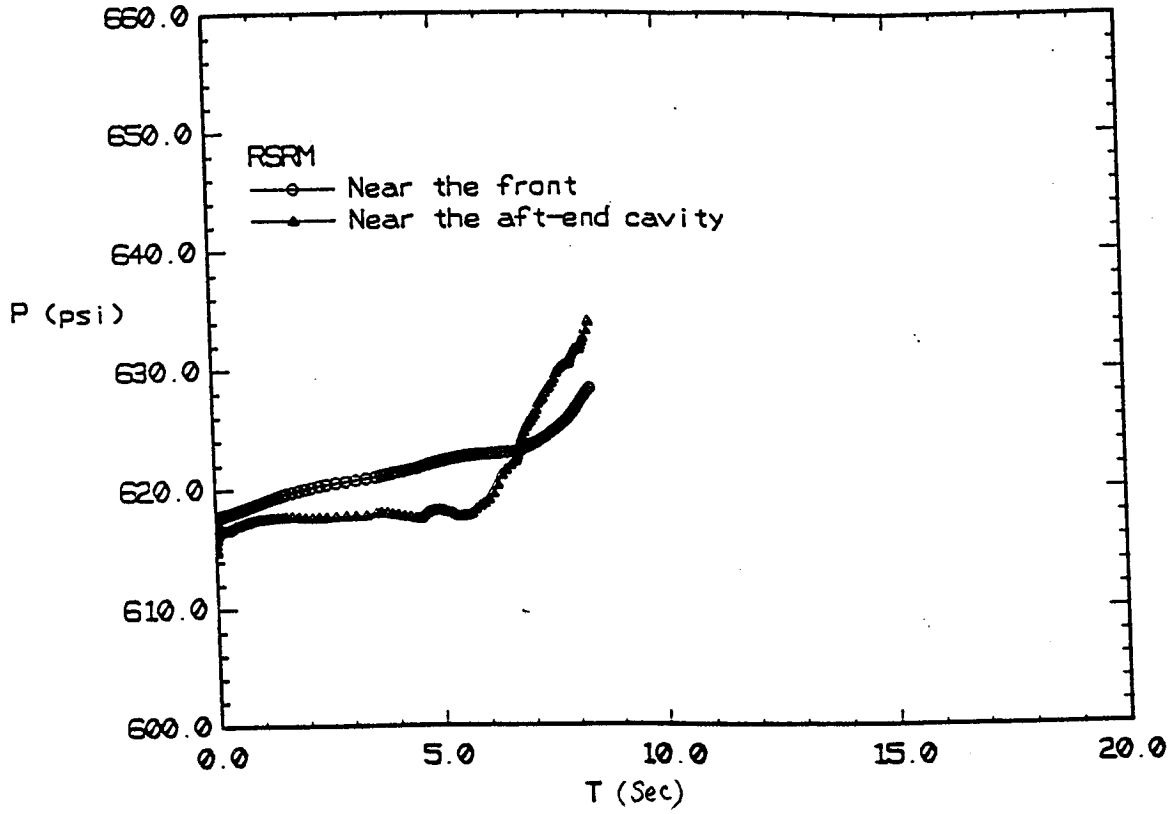

Figure 51 Pressure history due to the effect of slag buildup.

REPORT DOCUMENTATION PAGE

Form Approved
OMB No. 0704-0188

1. AGENCY USE ONLY (Leave blank)	2. REPORT DATE	3. REPORT TYPE AND DATES COVERED
	March 31, 1995	Contractor - Final

4. TITLE AND SUBTITLE

Advanced Multi-Phase Analysis for Solid Rocket Motors (SRMs)

5. FUNDING NUMBERS

NAS8-39398

6. AUTHOR(S)

Yen-Sen Chen and Paul Liaw

7. PERFORMING ORGANIZATION NAME(S) AND ADDRESS(ES)

Engineering Sciences, Inc.
1900 Golf Road, Suite D
Huntsville, AL 35802

8. PERFORMING ORGANIZATION REPORT NUMBER

9. SPONSORING/MONITORING AGENCY NAME(S) AND ADDRESS(ES)

George C. Marshall Space Flight Center
Marshall Space Flight Center, Al 35812

10. SPONSORING/MONITORING AGENCY REPORT NUMBER

11. SUPPLEMENTARY NOTES

D. Doran/Technical Monitor

12a. DISTRIBUTION/AVAILABILITY STATEMENT

unclassified - unlimited

12b. DISTRIBUTION CODE

13. ABSTRACT (Maximum 200 words)

The objective of this project is to develop an advanced particulate multi-phase flow model which include the effects of particle dynamics, chemical reaction and hot gas flow turbulence. The inclusion of particle agglomeration, particle/gas reaction and mass transfer, particle collision, coalence and breakup mechanisms in modeling the particle dynamics will allow the proposed model to realistically simulate the flowfield inside a solid rocket motor.

14. SUBJECT TERMS

Solid Rocket Motor, Multi-Phase Flow, Turbulence

15. NUMBER OF PAGES

65

16. PRICE CODE

17. SECURITY CLASSIFICATION OF REPORT	18. SECURITY CLASSIFICATION OF THIS PAGE	19. SECURITY CLASSIFICATION OF ABSTRACT	20. LIMITATION OF ABSTRACT
unclassified	unclassified	unclassified	unlimited